

STUDIES OF DESALTING SOLAR STILLS

Shigeki TOYAMA, Masaaki NAKAMURA, Kazunori MURASE
and Hassan Mohamed SALAH

Department of Chemical Engineering

(Received May 31, 1991)

Abstract

An extensive study has been conducted to develop a roof type solar still with wick attached below the heat penetrating plate which is feasible to compose multistage. First two sections deal with an establishment of mathematic simulation, and characterization of design parameters and operation variables on the basis of the simulation.

In the structure of stills, a sophisticated idea is required in the feeding system of liquid to the wick. Hence, the bended heat penetrating plate was invented, and the feasibility was proved.

Main structure of the still was a very flat rectangular enclosure where evaporation and condensation took place. Hence, the heat transfer mechanism was experimentally studied and provided instructive data for designing the still.

Finally, application for agricultural purposes in hot arid zones was discussed and the result quantitatively described the availability.

1. Simulation of a Multieffect Solar Still and the Static Characteristics

1.1. Introduction

Many attempts to develop solar stills have been reported as a means of utilizing local energy to solve water shortages, especially in isolated areas.^{1,2)} The basin type produces a little distillate and occupies a wide area and requires considerable investment for construction. On the other hand, the indirect type is designed so as to intensively utilize the absorbed solar energy but involves considerable expense due to the elaborate apparatus. Thus the principle of direct multieffect distillation is after all attractive.³⁾

The authors participated in a project to develop a multiple thermal-diffusion still with an ingenious idea,^{4,5)} and studied the process analysis. This section deals with an established mathematical model to simulate the process with experimental verification by a laboratory test plant. Design parameters and operation variables are also characterized.

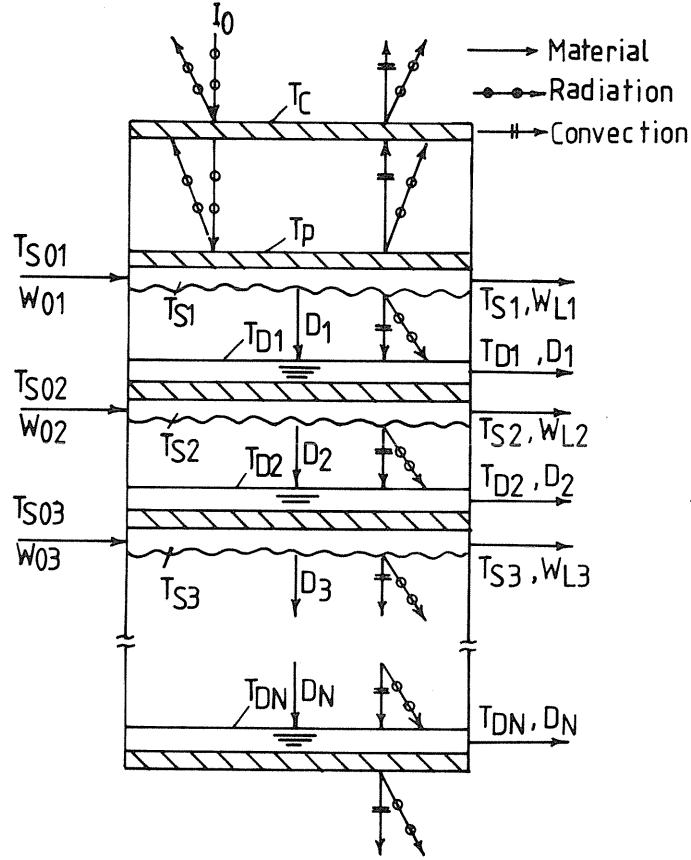


Fig. 1. 1. Flow directions of heat and mass through multi-effect solar still.

1. 2. Simulation Model of the Process

The flow of mass and heat for the direct multiple thermal-diffusion solar still is illustrated in Fig. 1. 1. The schematic diagram indicates a glass cover, a plate to receive solar radiation, partitions to separate the multiple stages and a heat-rejecting plate at the bottom. The specific points are to diffuse the solar energy from top to bottom by a process of evaporation and condensation in each stage and to feed liquid to be distilled through a porous sheet attached below each partition. While various models are conceivable to simulate this process, we assume here for simplicity that the temperature is constant in the direction of liquid flow. The heat and mass flows are indicated by arrows in Fig. 1. 1. Then the mathematical equations are formulated as follows:

Cover;

$$\begin{aligned}
 I_0 (\alpha_C + \tau_{CO_P} \alpha_C) - h_{PC} (T_P - T_C) \\
 + \varepsilon_P F_{PC} \sigma \{ (T_P + 273.15)^4 - (T_C + 273.15)^4 \} \\
 - h_{ca} (T_C - T_a) - \varepsilon_C F_{CS} \sigma \{ (T_C + 273.15)^4 \\
 - (T_{sky} + 273.15)^4 \} = 0
 \end{aligned} \tag{1}$$

Plate;

$$\begin{aligned}
 I_0 \tau_C \alpha_P - h_{PC} (T_P - T_C) - \varepsilon_P F_{PC} \sigma \{ (T_P + 273.15)^4 \\
 - (T_C + 273.15)^4 \} - U_1 (T_P - T_{S1}) = 0
 \end{aligned} \tag{2}$$

$$\begin{aligned}
 U_1 (T_P - T_{S1}) + W_{01} (C_{S01} T_{S01} - C_{S1} T_{S1}) \\
 - (W_{01} - W_{L1}) R_{S1} \\
 - \varepsilon_W F_{SD} \sigma \{ (T_{S1} + 273.15)^4 - (T_{D1} + 273.15)^4 \} \\
 - (K_1/Z_1) (T_{S1} - B_1 - T_{D1}) = 0
 \end{aligned} \tag{3}$$

Partition;

$$\begin{aligned}
 (W_{0i} - W_{Li}) R_{Di} + (K_i/Z_i) (T_{Si} - B_i - T_{Di}) \\
 + \varepsilon_W F_{SD} \sigma \{ (T_{Si} + 273.15)^4 - (T_{Di} + 273.15)^4 \} \\
 - U_{i+1} (T_{Di} - T_{Si+1}) = 0
 \end{aligned} \tag{4}$$

$$\begin{aligned}
 W_{0i+1} (C_{S0i+1} T_{S0i+1} - C_{Si+1} T_{Si+1}) \\
 - (W_{0i+1} - W_{Li+1}) R_{Si+1} + U_{i+1} (T_{Di} - T_{Si+1}) \\
 - \varepsilon_W F_{SD} \sigma \{ (T_{Si+1} + 273.15)^4 - (T_{Di+1} + 273.15)^4 \} \\
 - (K_{i+1}/Z_{i+1}) (T_{Si+1} - B_{i+1} - T_{Di+1}) = 0
 \end{aligned} \tag{5}$$

$$\begin{aligned}
 (W_{0i} - W_{Li}) - \{ (D_i/Z_i a_i) \} (P_{Si} - P_{Di}) / P_{Bmi} = 0 \\
 (i = 1, 2, \dots, N-1)
 \end{aligned} \tag{6}$$

where;

$$P_{Bmi} = \frac{(P_{Si} - P_{Di})}{\ln \left(\frac{\pi - P_{Di}}{\pi - P_{Si}} \right)}$$

Heat rejector;

$$\begin{aligned} & (W_{0N} - W_{LN})R_{DN} + (K_N/Z_N)(T_{SN} - B_N - T_{DN}) \\ & + \varepsilon_W F_{SD} \sigma \{(T_{SN} + 273.15)^4 - (T_{DN} + 273.15)^4\} \\ & - U_{rad}(T_{DN} - T_a) = 0 \end{aligned} \quad (7)$$

$$(W_{0N} - W_{LN}) - \{(D_N/Z_N \cdot a_N)\}(P_{SN} - P_{DN})/P_{BMN} = 0 \quad (8)$$

Any leakage of material and thermal heat loss from each frame between partitions are neglected, and filmwise condensation is assumed. There are $(3N + 2)$ algebraic equations, so that the following $(3N + 2)$ unknowns were selected to characterize the process.

$$\begin{array}{cccc} (T_P, T_C), & W_{L1}, & T_{S1}, & T_{D1} \\ & W_{L2}, & T_{S2}, & T_{D2} \\ & \vdots & \vdots & \vdots \\ & W_{Li}, & T_{Si}, & T_{Di} \\ & \vdots & \vdots & \vdots \\ & W_{LN}, & T_{SN}, & T_{DN} \end{array}$$

These unknowns are calculated by the Newton-Raphson iteration method. The sequence of commands is:

- 1) Set parameters.
- 2) Assume starting values for variables.
- 3) Compute residues.
- 4) Compute the elements of Jacobian matrix.
- 5) Compute the product of Jacobian matrix inverse and residues vector.
- 6) Compute the values of variables for the current iteration.
- 7) Relax the values of variables by applying suitable relaxation method.
- 8) If the convergence is sufficient, print the results.
- 9) If convergence not sufficient, go to step 3).

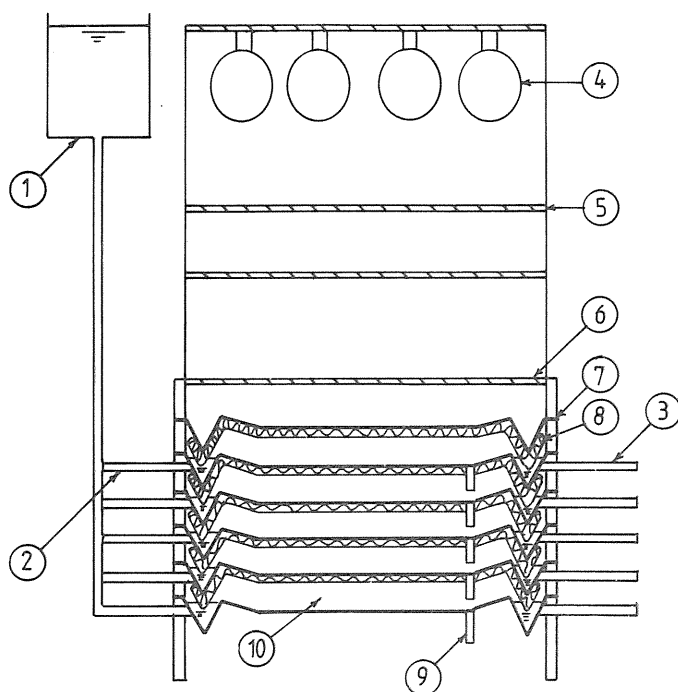


Fig. 1. 2. Experimental apparatus: 1. overhead tank; 2. feeder; 3. outlet water tube; 4. infrared lamp; 5. smoked glass sheet; 6. glass cover; 7. metal plate; 8. fibrous sheet; 9. distillate outlet tube; 10. diffusion gap.

1. 3. Experimental Apparatus with a Laboratory Test Plant

The main components of the experimental apparatus are five successive parallel stages constructed from metal sheets (0.5 mm thick) as shown in Fig. 1. 2. Each stage has a length of 1 m and a width of 1 m with a diffusion gap of 10 mm. Water as the liquid to be evaporated is fed to each stage by a system incorporating pump, overhead tank, V-shaped feeder, wick, etc. The water is sucked from the V-shaped feeder and permeates through the wick under the effect of inclination. The apparatus was mounted on an angle-iron frame and irradiated by an overhead array of sixteen infrared lamps. The maximum power of each lamp was 250 W at 100 V.

Two smoked glass sheets were installed as a filter (0.3 m) below the lamp housing, and reflecting panels were attached vertically to the ends and sides. Thus, the heating intensity was sustained uniformly over the plate.

The power of the lamps was adjusted using laboratory transformers and the radiation intensity was measured by a pyranometer Model (MS-42). The temperature distributions of water passing through each fibrous sheet in the direction of flow were measured at distance of $x=0, 0.25, 0.5, 0.75$ and 1 m by using copper-constantan thermocouples of 0.25 mm diameter.

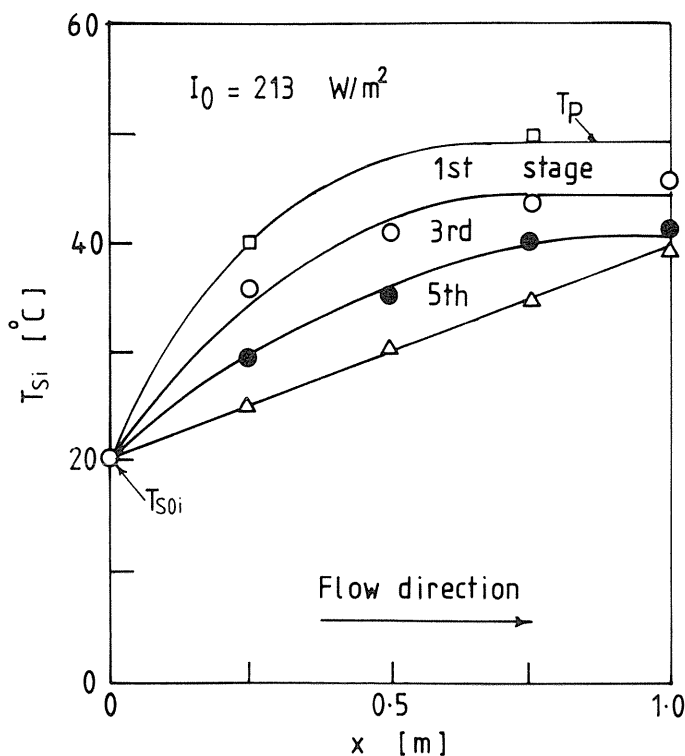


Fig. 1. 3. Water temperature distribution in direction of flow at each effect.

Typical temperature profiles are shown in Fig. 1. 3. It can be seen that the temperature distribution approaches the isothermal condition at small distances from the inlet for the top stages but that the non-isothermal zone increases toward the bottom stages. This is interpreted to mean that the energy input to the top stage is enough to establish equilibrium conditions at a small distance from inlet and most can be effectively utilized in the evaporation process of it but that the input energy to the bottom stage is so small that a considerable part is utilized in raising the enthalpy of the flowing water.

Two groups of 6 junction, 0.25 mm diameter copper-constantan thermocouples were attached to each condensating plate to obtain the average temperature of condensate. Also, the average temperature of water passing through fibrous sheet of each stage was obtained from the measured temperature distribution. Representative temperatures at each stage are shown in Fig. 1. 4A. and Fig. 1. 5A. It is clear from the figures that the temperature difference through partitions is maximum for the upper stage and decreases toward the bottom stage. The computed temperatures shown by solid lines also indicate good agreement with experiments. The measured temperature of the upper plate shows a value higher than the computed one due to the effect of radiation on the thermocouple junction.

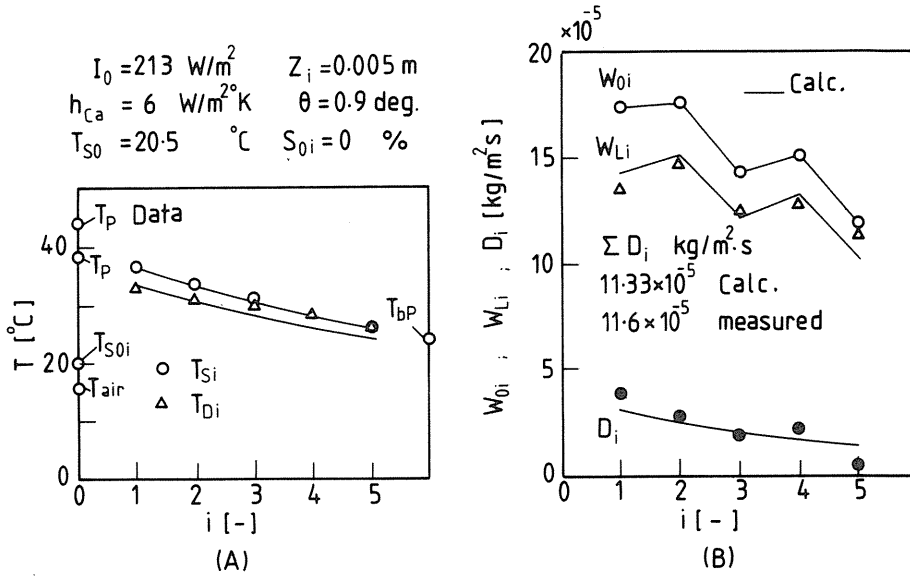


Fig. 1. 4. Temperature and distillate productivity distributions for successive stages.

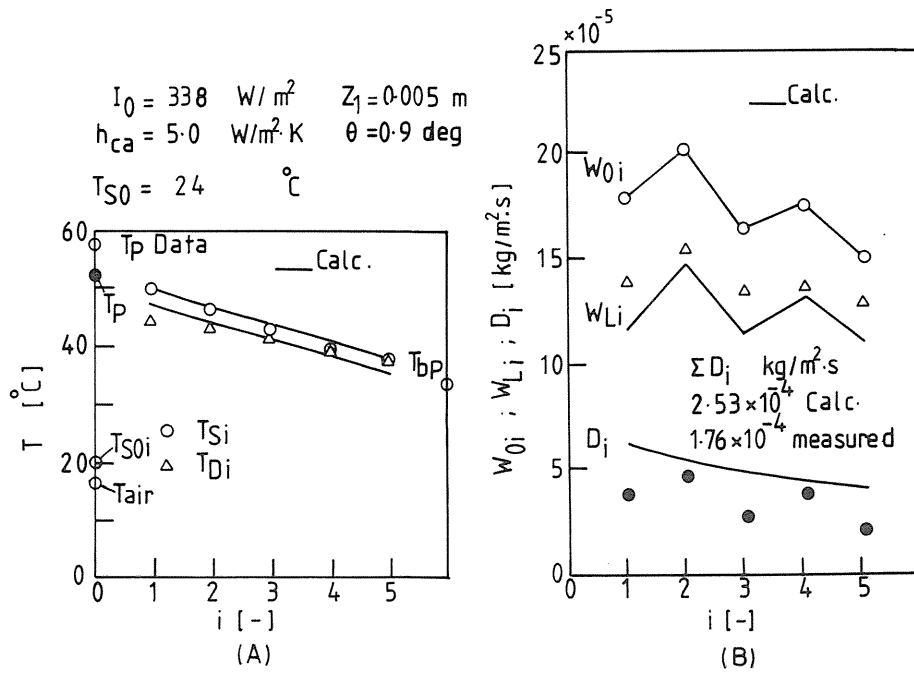


Fig. 1. 5. Temperature and distillate productivity distributions for successive stages.

Table 1. 1. Physical properties and constants.

Latent heat of water ⁷⁾	
$R_D = 2.3246 \times 10^3 (1.0727 \times 10^3 - 1.0167 T_D + 1.4087 \times 10^{-4} T_D^2 - 5.1462 \times 10^{-6} T_D^3)$	[J/kg]
Latent heat of brine ⁷⁾	
R_S : The same as in equation above at $T_D = T_S$	
Heat capacity of brine ⁷⁾	
$C_s = (4.2055 - 0.0678 S \times 1.4757 \times 10^{-3} S^2) \times 10^3 - (13.604 - 6.1917 S + 0.3251 S^2) \times 10^2 T_S + (15.908 - 5.0572 S + 0.2562 S^2) \times 10^{-3} T_S^2$	[J/kg · K]
Boiling point elevation ⁸⁾	
$B = (0.528764 \times 10^{-1} + 0.82603 \times 10^{-3} T_S - 0.315082 \times 10^{-7} T_S^2) S + (0.320553 \times 10^{-2} - 0.144367 \times 10^{-4} T_S + 0.184416 \times 10^{-6} T_S^2) S^2$	[°C]
Vapor pressure of water (Antonie Equation) ⁹⁾	
$p = 133.32 \exp \{18.6686 - 4030.1824 / (T + 235.15)\}$	[N/m ²]
Heat capacity of air ⁹⁾	
$C_{air} = 0.9992 \times 10^3 + 1.4319 \times 10^{-1} T_A + 1.1010 \times 10^{-4} T_A^2 - 6.7851 \times 10^{-8} T_A^3$	[J/kg · K]
Thermal conductivity of air ⁹⁾	
$K = 0.0244 + 0.7673 \times 10^{-4} T_i$	[W/m · K]
Viscosity of air ⁹⁾	
$\mu = 1.718 \times 10^{-5} + 4.620 \times 10^{-8} T_i$	[N · s/m ²]
Diffusivity of steam through air ⁹⁾	
$\nu = 7.7255 \times 10^{-10} (T + T_C)^{1.83}$	[m ² /s]
Expansion factor of air	
$\beta = 1 / (T + 273.15), \quad T = (T_p + T_C) / 2$	[1/K]
Gravitational acceleration	
$g = 9.81$	[m/s ²]
Radiation properties	
$\alpha_C = 0.85, \quad \alpha_P = 0.95, \quad \alpha_W = 0.87, \quad \tau_C = 0.92, \quad \rho_P = 0.05, \quad F_{pc} = 1.0, \quad F_{CS} = 1.0, \quad F_{SD} = 1.0$	[—]
Heat convection relation ⁹⁾	
$h_{pC} = K / Z_0 C (P_r G_r)^n$	
where	
$C = 0.21, \quad n = 1/4 \quad \text{for } 10^4 < Gr < 3.2 \times 10^5$	
$C = 0.075, \quad n = 1/3 \quad \text{for } 3.2 \times 10^5 < Gr < 10^7$	
Pr : Prandtl number, $C_{air} \mu / k$	
Gr : Grashof number, $Z_0^3 \sigma^2 g \beta (T_p - T_C) / \mu^2$	
Cover to air convection relation ²⁾	
$h_{ca} = 5.7 + 3.8 \nu$	[W/m ² · K]
Sky temperature ²⁾	
$T_{sky} = (T_A + 273.15)(0.55 + 5.671 \times 10^{-3} \sqrt{f P_A})^{0.25} - 273.15$	[°C]

The mass balance for each stage was obtained under certain operating conditions after attaining steady-state conditions, which took about 7 h. The typical mass balances for the different stages are shown in Fig. 1. 4B. and Fig. 1. 5B. for, respectively, $I_0 = 213 \text{ W/m}^2$ and $I_0 = 338 \text{ W/m}^2$. The solid lines also indicate the calculated values, which show good agreement with the experimental values at lower values of heat intensity as shown in Fig. 1. 4B. Overprediction is noticed at the condition of high intensity and this may be attributed to the partial drying of fibrous sheet at higher heat intensity. The liquid feed system in such apparatus will be independently discussed in another paper.

1. 4. Process Characterization

The series of experiments proved that the mathematical model developed in this study is practically usable for the simulation of solar stills. Hence the design parameters and operation variables were characterized by simulation with the model for the cases of practical sea water desalination. The numerical values for constants and physical properties in the mathematical equations are given in Table 1. 1., keeping in mind the need to meet generality. The number of stages is normally fixed at 10 because solar radiation is usually stronger than as compared with the laboratory test radiation.

1. 4. 1. Weather conditions

The solar intensity and the heat transfer coefficient at the outer plate as a measure of wind velocity are taken as representative parameters of weather condition. Their effects on the distilled water productivity are shown in Fig. 1. 6. As has been pointed out in published papers^{1,6)} for simple basin types, the significance of solar intensity and less sensitivity to wind are also revealed for such a multieffect process. Circles at the end of curves indicate dry over points of brine.

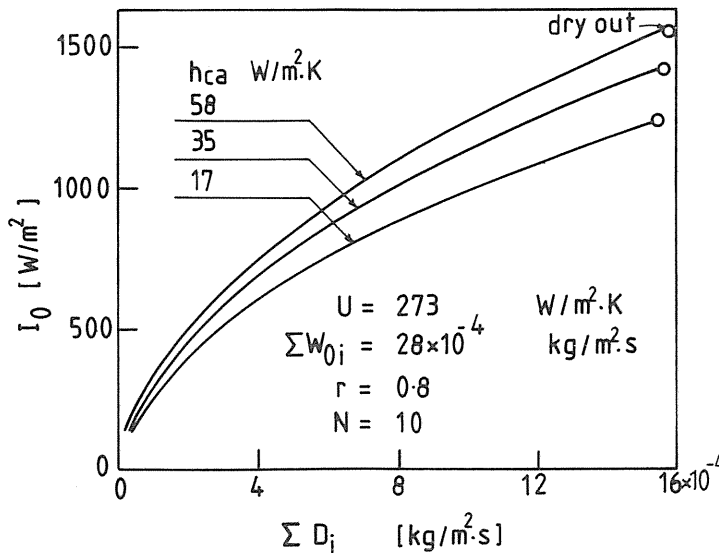


Fig. 1. 6. Effect of weather conditions on water productivity.

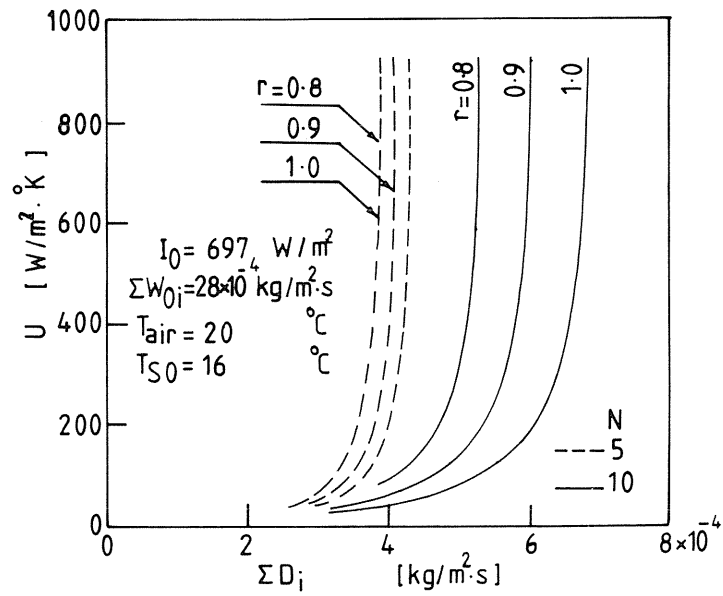


Fig. 1. 7. Effect of overall heat transfer coefficient through partition on distillate productivity.

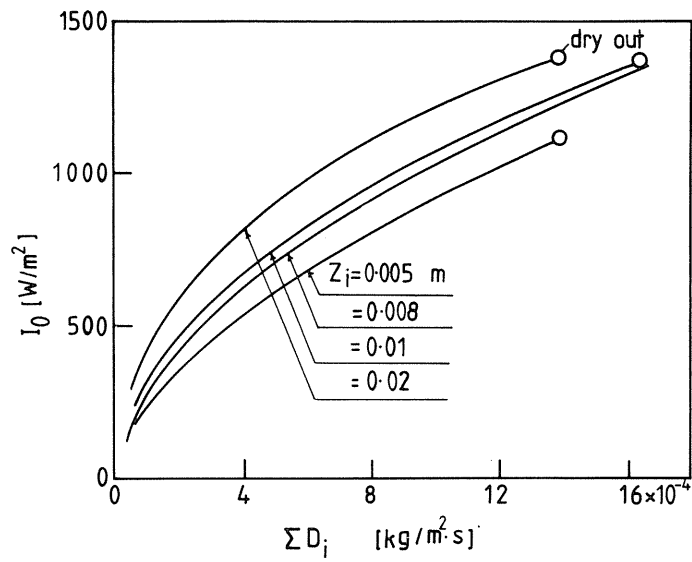


Fig. 1. 8. Effect of diffusion gap on distillate productivity.

1.4.2. Design parameters

The overall heat transfer coefficient through the partition is a significant parameter since it is related to the material choice for partitions and holding structure of liquid films along both sides. The calculated results are plotted against the number of partitions, which is a basic parameter of such a multieffect type as is shown in Fig. 1. 7. The figure shows that the water productivity becomes flat at higher heat transfer coefficient. The trend is more distinct for a smaller number of partitions. For example, in the case of $N=5$ the water productivity becomes almost flat at $U = 230 \text{ W/m}^2 \cdot \text{K}$.

Fig. 1. 8. shows the effect of the clearance between partitions as vapor diffusion gap on the productivity. It is clear that for intensity lower than 350 W/m^2 the productivity is independent of the clearance. Then the productivity increases with decreasing clearance size and

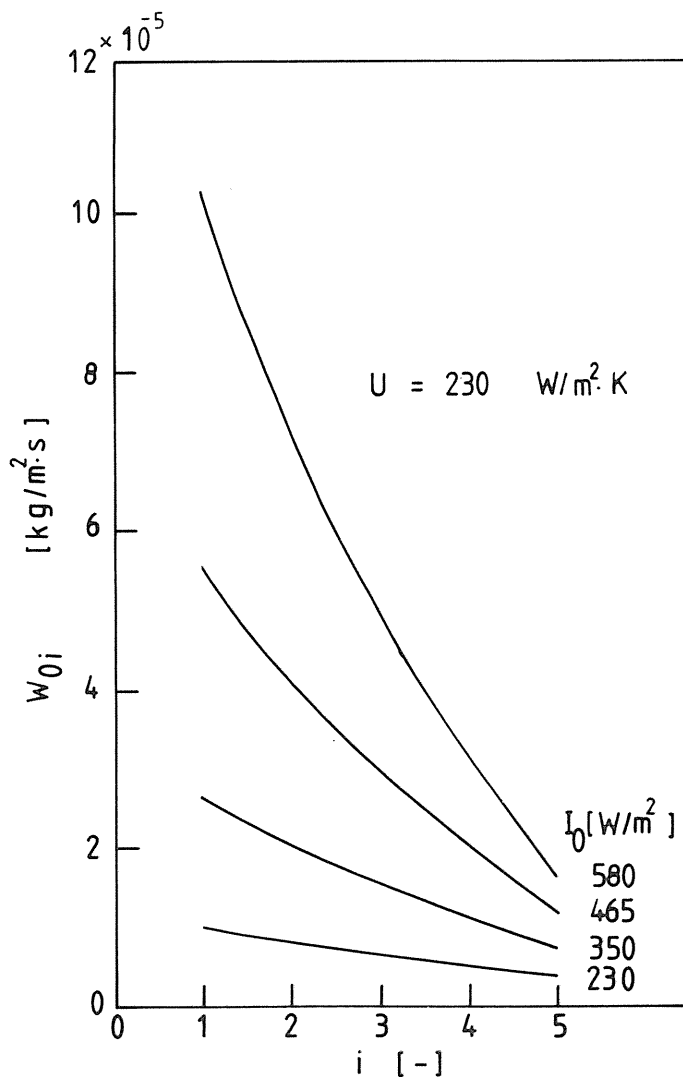


Fig. 1. 9 Feed rate distribution for maximum distillate productivity at different values of solar intensity.

with increasing solar intensity. The effect of inclination on the receiving plate will be extrapolated from the dependence of solar intensity. Also, the clearance will depend on the capability of manufacturing, and the optimum N will be decided after the cost parameter becomes definite.

1. 4. 3. Operation variable

The productivity of solar stills is mainly determined by uncontrollable weather conditions. The only controllable operation variable is feed rate, which should be determined to maximize the distillate productivity. The objective function is given by:

$$J = \sum_{i=1}^N [W_{0i} - W_{Li}]^2 - \alpha [W_{0i} - W_{0i}^*]^2 \quad (9)$$

Practical desalination of sea water requires operational restrictions to prevent scale formation, which depends on the solubility of gypsum. This restriction is given as:

$$\begin{aligned} S_i/S_{0i} = W_{0i}/W_{Li} = 2.4125 \times 10^{-4} T_{Si}^2 - 7.0425 \\ \times 10^{-2} T_{Si} + 6.09 \end{aligned} \quad (10)$$

This constrained optimization was calculated by applying the simplex method. The result is shown in Fig. 1-9 for various solar intensities as a parameter. This result showed that feed rates at the subsequent stages can be expressed by geometrical series with ratio $r = 0.7 \pm 0.1$ as follows:

$$W_{0i} = W_{01} \times r^{i-1} \quad i(1, 2, \dots, N) \quad (11)$$

function of the solar intensity as:

$$W_{01} = 1.22 I^{2.5} \quad (12)$$

Such an expression will be convenient for practical operation although the numerical values are inherent to this case study.

1. 5. Conclusion

A simulation model for multieffect thermal-diffusion stills has been presented. Calculations made with this model agreed favorably with experimental measurements obtained by a laboratory test plant.

The results showed that productivity of distillate becomes independent of the overall heat transfer coefficient through partition when its value becomes higher than $230 \text{ W/m}^2 \cdot \text{K}$.

The productivity increases with increasing solar intensity and decreasing gap thickness but becomes independent of the gap thickness when solar intensity is less than 350 W/m^2 .

The optimum feed rate of brine to each stage to maximize the distillate productivity was also calculated by the simplex method. The result showed that the feed to the first stage is proportional to the solar intensity by the power of 2.5 and the feed rates to the subsequent stages are expressed by geometrical series with a ratio of about 0.7.

2. Dynamic Characteristics of a Multistage Thermal Diffusion Type Solar Distillator

2.1. Introduction

A multiple thermal stage diffusion type distillator has been developed^{3,4)} and the static characteristics were extensively studied¹⁰⁾ for parameters such as the basic process variables and weather conditions. The established computer model was also experimentally verified. This section extended the simulation model to unsteady state and elucidated dynamic behaviour of the process.

The calculated results including sensitivity analysis and the effect of a specific design parameters could provide an useful information to the process development.

2.2. Dynamic Simulation Model of the Process

The flow of mass and heat for the direct multiple thermal diffusion type solar distillator is illustrated in Fig. 2. 1.

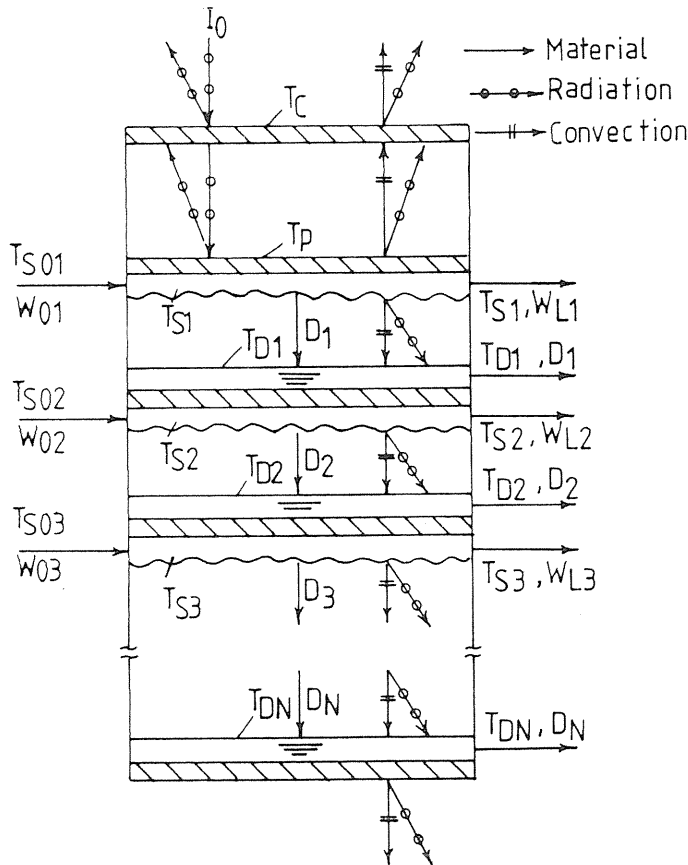


Fig. 2. 1. Energy and mass transfer paths in a multistage thermal diffusion type solar distillator.

The schematic diagram indicates a glass cover, a plate to receive solar beam, and partitions to perform the multiple stage and a heat rejecting plate at the bottom. The specific points are to diffuse the solar energy from upper to bottom by the process of evaporation and condensation in each stage and to feed the liquid to be distilled through a porous sheet attached below each partition. While various models would be conceivable to simulate this process, we assume here for simplicity that the temperature is constant along the liquid flow direction. The heat and mass flows are indicated by arrows in Fig. 2. 1. Then the mathematical equations are formulated as follow:

Cover;

$$I_0 (\alpha_c + \tau_{cOp} \alpha_c) + h_{pC} (T_P - T_C) + \varepsilon_p F_{pC} \sigma (T_P^4 - T_C^4) - h_{ca} (T_C - T_a) - \varepsilon_c F_{cS} \sigma (T_C^4 - T_{sky}^4) = m_c C_c dT_C / dt \quad (1)$$

Plate;

$$I_0 \tau_c \alpha_p - h_{pC} (T_P - T_C) - \varepsilon_p F_{pC} \sigma (T_P^4 - T_C^4) - U_{S1} (T_P - T_{S1}) = m_p C_p dT_P / dt \quad (2)$$

Evaporator;

$$U_{Si} (T_{Pi-1} - T_{Si}) + W_{0i} (C_{S0i} T_{S0i}) - W_{Li} (C_{Si} T_{Si}) - D_i R_{Si} - C_{Di} T_{Si} D_i - \varepsilon_w F_{SD} \sigma (T_{Si}^4 - T_{Di}^4) - (k_i / z_i) (T_{Si} - B_i - T_{Di}) = m_{Si} C_{Si} dT_{Si} / dt$$

$$\text{For } i = 1 \text{ put } T_{Pi-1} = T_P \quad (3)$$

Condensate;

$$D_i R_{Di} + \varepsilon_w F_{SD} \sigma (T_{Si}^4 - T_{Di}^4) - U_{Di} (T_{Di} - T_{Pi}) + (k_i / z_i) (T_{Si} - B_i - T_{Di}) = m_{Di} C_{Di} dT_{Di} / dt \quad (4)$$

Plate;

$$U_{Di} (T_{Di} - T_{Pi}) - U_{Si} (T_{Pi} - T_{Si+1}) = m_{Pi} C_{Pi} dT_{Pi} / dt \quad (5)$$

$$(i = 1, 2, 3, \dots, N-1) \quad (6)$$

Heat Rejector;

$$U_{DN} (T_{DN} - T_{PN}) - h_{ra} (T_{PN} - T_a) = m_{PN} C_{PN} dT_{PN} / dt \quad (7)$$

$$D_i - \{(D_i/Z_i a_i)\} (P_{Si} - P_{Di})/P_{Bmi} = 0$$

$$(i = 1, 2, 3, \dots, N) \quad (8)$$

where;

$$P_{Bmi} = \frac{(P_{Si} - P_{Di})}{\ln \left(\frac{\pi - P_{Di}}{\pi - P_{Si}} \right)} \quad (9)$$

Where any leakage of material and thermal heat loss from each frame between partitions are neglected and film wise condensation is also assumed. These are composed of $(3N + 2)$ first order differential equations and the unknowns are the temperatures of the different components of the distillator. The equations were solved simultaneously by using Runge-Kutta Method.

2. 3. Model verification by a Laboratory Test Plant and the Characterization

2. 3. 1. Simulation of a laboratory test plant

A laboratory test plant having 5 stages with 1 m^2 in frame area was heated by electric lamps and the response to stepwise change of heating intensity was measured. A typical result is shown in Fig. 2. 2 together with the computed curve for the same condition as discribed in the figure.

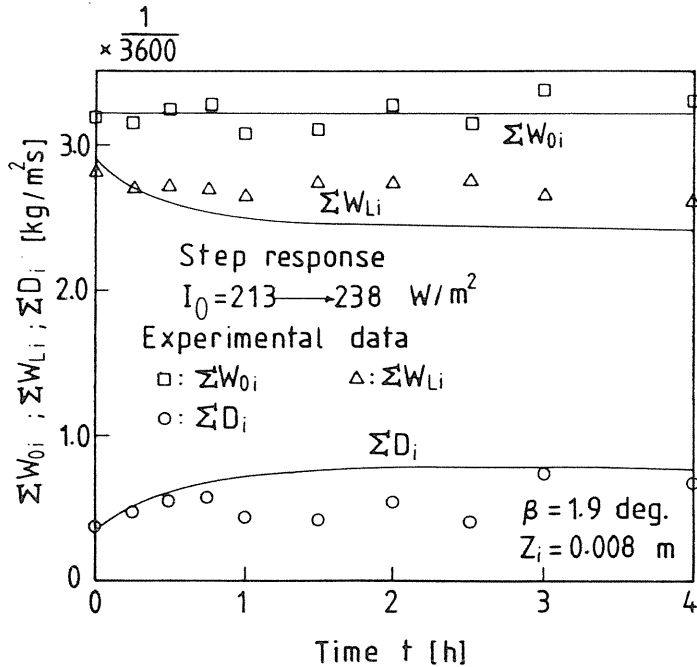


Fig. 2. 2. Response to stepwise change of heating intensity for the laboratory distillator.

In such a laboratory test, the heating condition was freely controllable. Meanwhile, strong heating was so difficult to apply that a considerable error was predicted due to the heat loss from the surface which could not be precisely estimated. In taking this into account, the calculated result was agreed fairly well with the experimental data.

2. 3. 2. The dynamic characteristics

The calculated curve is approximately identified to a first order system as given by:

$$G(s) = \frac{K}{1 + T^*s} \quad (10)$$

where;

$$K = \frac{\Delta(\Sigma D)}{\Delta I} \quad (11)$$

The gain constant K and time constant T^* were calculated for various indicial changes. The result is shown in Fig. 2. 3 for different stage interval which is the most sensitive design parameter.

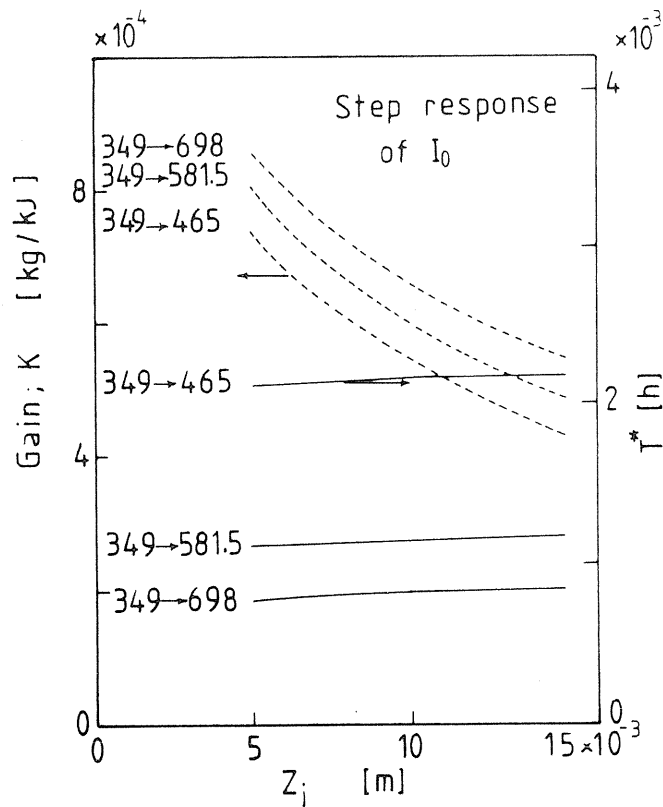


Fig. 2. 3. Constants in first order system versus stage interval for different stepwise changes of heating intensity.

Responses to other parameters such as feed rate and sea water temperature were also approximated by Equation (10), but they were not so significant as to describe here. The response to the change of ambient temperature, however, was differed as shown in Fig. 2. 4. The initial increase of produced distillate is due to expansion of the effective temperature span. The gradual decrease is caused by total quenching of the distillator.

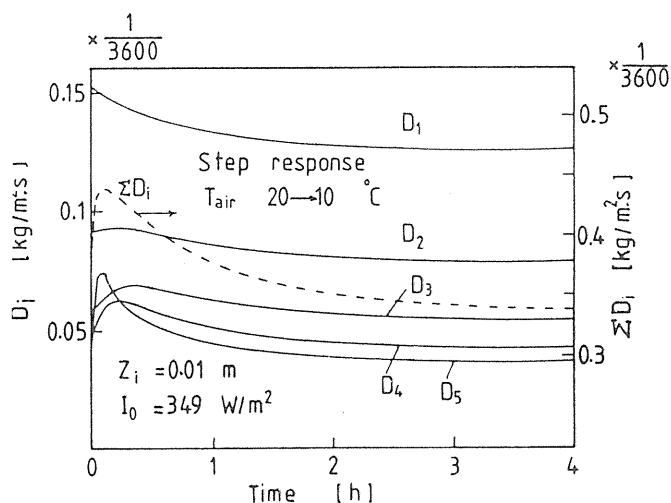


Fig. 2. 4. The response to the change of ambient temperature for the laboratory distillator.

2. 4. Model Verification by a Field Test Plant and the Characterization

2. 4. 1. Simulation of a field test plant

Field test plants having 10 stages with 3 m² in frame area were installed in Okinawa island, Japan, by Water Reuse Promotion Center and conducted a series of experiments. The data obtained in such a field test were usually taken at less stable conditions and with insufficient observation. A set of data was selected among them as to be available enough for applying to the computer simulation. The process condition are given in Table 2. 1 and the weather condition is in Table 2. 2. The simulated result is shown in Fig. 2. 5. The calculated values agreed sufficiently with the experimental one.

2. 4. 2 Extension of the model to case studies

Computation of the dynamic model was so considerably time consumptive that we were unable to apply extensive optimum searching technique. A series of empirical case studies were, therefore, carried out under the following conditions.

1. Solar radiation was variated sinusoidally with time and it was calculated by using the measured maximum value of solar intensity observed in certain place along the Red Sea (Egypt) in four sample days. They were 938.0 W/m² in March, 942.5 W/m² in June, 906.5 W/m² in September and 798.2 W/m² in December.
2. Patterns of ambient temperature change through the day were taken from observed data at the same place in Egypt.

Table 2. 1. Physical properties and constants.

Latent heat of water ⁷⁾	
$R_D = 2.3246 (1.0727 \times 10^3 - 1.0167 T_D + 1.4087 \times 10^{-4} T_D^2 - 5.1462 \times 10^{-6} T_D^3)$	[kJ/kg]
Latent heat of brine ⁷⁾	
R_S : The same as above equation above at $T_D = T_S$	
Heat capacity of brine ⁷⁾	
$C_s = (4.2055 - 0.0678 S \times 1.4757 \times 10^{-3} S^2) - (13.604 - 6.1917 S + 0.3251 S^2) \times 10^{-4} T_S + (15.908 - 5.05972 S + 0.2562 S^2) \times 10^{-3} T_S^2$	[kJ/kg · K]
Boiling point elevation ⁸⁾	
$B = (0.528764 \times 10^{-1} + 0.82603 \times 10^{-3} T_S - 0.315082 \times 10^{-7} T_S^2) S + (0.320553 \times 10^{-2} - 0.144367 \times 10^{-4} T_S + 0.184416 \times 10^{-6} T_S^2) S^2$	[°C]
Vapor pressure of water (Antonie Equation) ⁹⁾	
$p = 133.32 \exp \{18.6686 - 4030.1824 / (T + 235.15)\}$	[N/m ²]
Heat capacity of air ⁹⁾	
$C_{air} = 0.97 + 6.788 \times 10^{-5} T_A + 16.5768 \times 10^{-8} T_A^2 - 6.7880 \times 10^{-11} T_A^3$	[kJ/kg · K]
Thermal conductivity of air ⁹⁾	
$K = 0.0244 + 0.7673 \times 10^{-4} T_i$	[W/m · K]
Viscosity of air ⁹⁾	
$\mu = 1.718 \times 10^{-5} + 4.620 \times 10^{-8} T_i$	[Pa · s]
Diffusivity of steam through air ⁹⁾	
$\phi = 7.7255 \times 10^{-10} T_i^{1.83}$	[m ² /s]
Density of air at $\pi = 1.0132 \times 10^{-5}$ N/m ²	
$\rho = 353.44 / T_A$	[kg/m ³]
Expansion factor of air	
$\beta = 1 / T_A$	[1/K]
Gravitational acceleration	
$g = 9.81$	[m/s ²]
Radiation properties	
$\alpha_C = 0.85, \alpha_P = 0.95, \alpha_W = 0.87, \tau_C = 0.92, \rho_P = 0.05, F_{pe} = 1.0, F_{CS} = 1.0, F_{SD} = 1.0$	[-]
Heat convection relation	
$h_{pC} = K / Z_0 C (Pr Gr)^n$	
where	
$C = 0.21, n = 1/4 \quad 10^4 < Gr < 3.2 \times 10^5$	
$C = 0.075, n = 1/3 \quad 3.2 \times 10^5 < Gr < 10^7$	
Pr : Prandtl number, $C_{air} \mu / k$	
Gr : Grashof number, $Z_0^3 \rho^2 g \beta (T_p - T_C) / \mu^2$	
Cover to air convection relation ²⁾	
$h_{ca} = 5.7 + 3.8 \nu$	[W/m ² · K]
Sky temperature ²⁾	
$T_{sky} = (T_A + 273.15)(0.55 + 5.671 \times 10^{-3} \sqrt{f P_A})^{0.25} - 273.15$	[°C]

Table 2. 2. Weather condition for field test.

t (h)	9–10	10–11	11–12	12–13	13–14	14–15	15–16	16–17
I_0 (W/m^2)	395.18	611.85	666.28	730	779	713	452.6	125.0
T ($^{\circ}\text{C}$)	22.3	22.8	22.8	22.5	22.9	22.8	22.6	21.6

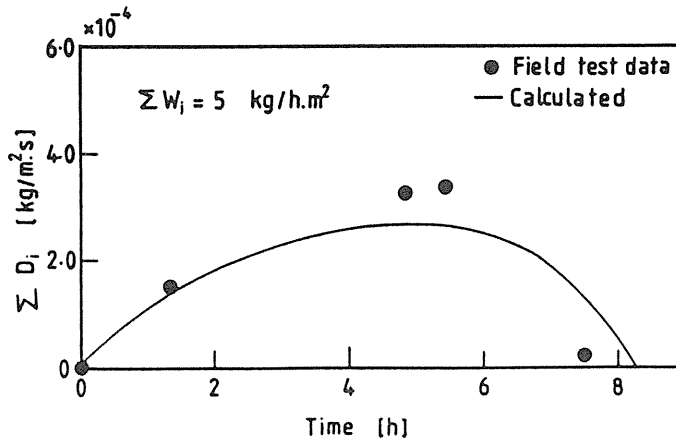


Fig. 2. 5. Variations of the distillate production rate with time after 9 o'clock.

- Physical properties and design parameters are shown in Table 1.
- Sea water temperature was assumed to be uniform over the day and varying through the year. The used values were 24.5°C in March, 28.5°C in June, 32.5°C in September and 27.5 in December.

Scheduling of brine feed was studied as an important controllable parameter. Three feed rates, namely, F_1 for t_1 after sun rise, F_2 for subsequent t_2 and F_3 until sun set as shown in Fig. 2. 6 were determined to optimize the distillate productivity under the following restriction to the salt concentration.

$$S^*/S_0 = 6.527 \exp(-0.015 T_S) \quad (12)$$

The results at four sample days throughout the year are given in Table 2. 3. It is noticeable that this type of 5 effects distillator can give about 7 times the productivity of a conventional solar basin, if the brine feed would be optimally scheduled.

2. 4. 3. Sensitivity of distillate productivity to process parameters

Sensitivities to the distillate productivity were calculated for process parameters such as intensity of solar radiation, ambient temperature and sea water temperature. The September operating condition was selected as the standard and the results are shown in Table 2. 4. Tendencies for a big change of these parameters are also shown in Figs. 2. 7, 2. 8 and 2. 9 to get a practical image although their range are not always realistic.

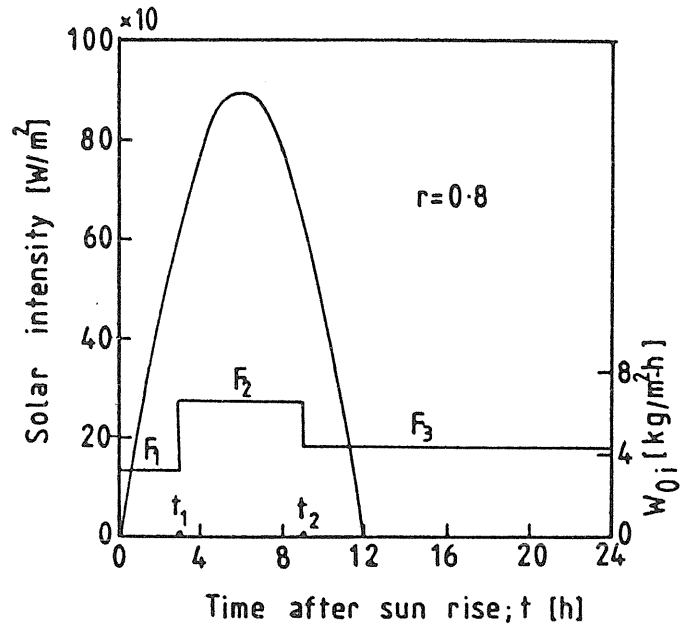


Fig. 2. 6. Variation of solar intensity with operation time and scheduling of brine feed.

Table 2. 3. Performance and operation parameters for sample days in certain location at Red Sea in Egypt.

	t_1 (h)	t_2 (h)	F_1	F_2 (kg/h)	F_3	T_a (°C)	T_{s0} (°C)	H_s (kJ/m ² · day)	Productivity (kg/m ² · day)
March	3.0	9.0	3.4	6.6	4.0	30	24.5	25,810	20.33
June	3.0	12.0	3.6	6.8	0.6	35	28.5	25,934	21.47
Sept.	3.0	9.0	3.2	6.6	4.4	29.5	32.5	24,940	20.86
Dec.	3.0	9.0	2.4	5.2	3.0	25.0	27.5	21,953	16.75

Table 2. 4. Sensitivity of the productivity to the process parameters.

$\partial D / \partial T_s$	0.24	$\partial D / \partial F_1$	-0.1033
$\partial D / \partial T_a$	0.112	$\partial D / \partial F_2$	-0.736
$\partial D / \partial H_s$	0.24×10^{-3}	$\partial D / \partial F_3$	-0.07

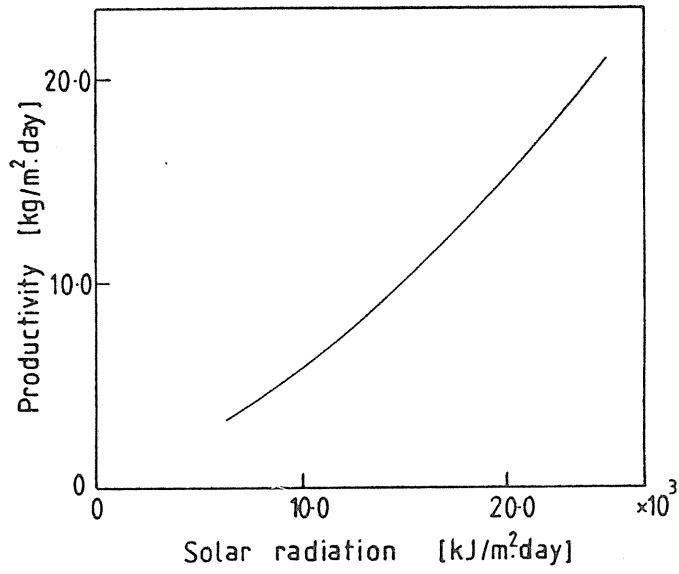


Fig. 2. 7. Effect of solar radiation on productivity.

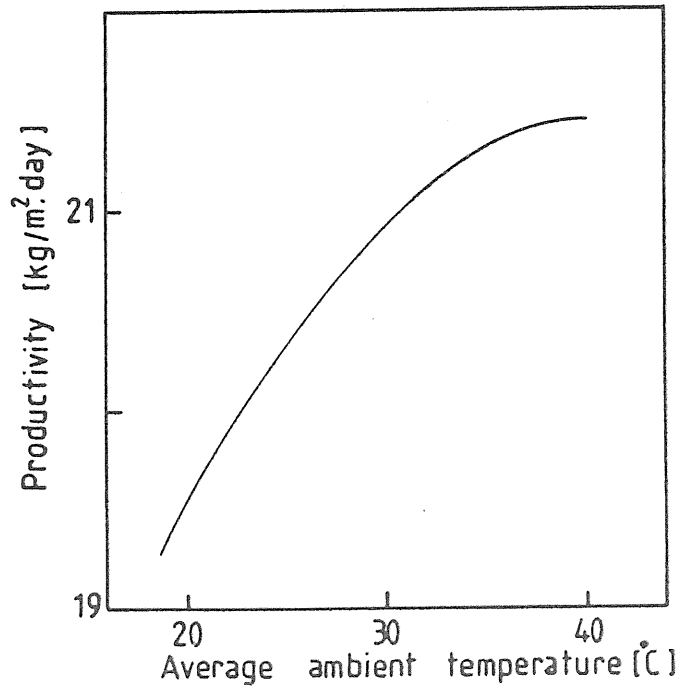


Fig. 2. 8. Effect of average ambient temperature on productivity.

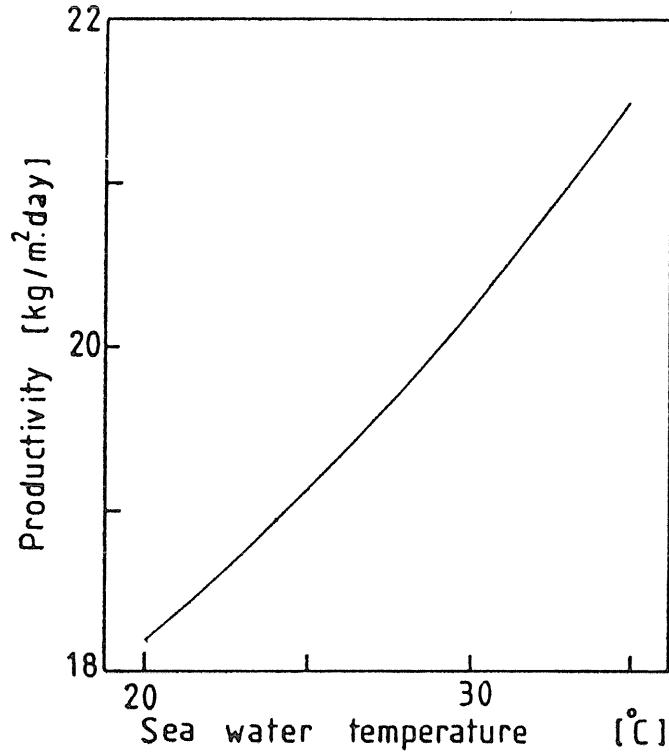


Fig. 2. 9. Effect of sea water temperature on productivity.

2. 4. 4. Performance with concrete slab

The upper plate of the distillator is severely subjected to thermal stress, and requests high durability to hot sea water.

Therefore the aim of this section is to study the performance of the distillator when replacing the upper plate with concrete slab. The differential equation which governs the heat flow inside slab can be written as follow:

$$\frac{\partial T_p}{\partial t} = \lambda_c \frac{\partial^2 T_p}{\partial y^2} \quad (13)$$

Approximating the right hand side of this equation by finite difference we can get another set of first order differential equations. Replacing equation (2) with the set of equations were can solve simultaneously by Runge-Kutta Method.

The weather conditions in September were selected as the input data for this calculations. Scheduling of feed which is required to maximize the distillate productivity is shown in Table 2. 5. Variations of the temperature difference emerged on the concrete slab and the distillator with five stages are shown in Fig. 2. 10.

The variation of distillate rate with time for the distillator with concrete slab are shown in Fig. 2. 11 in comparison with that of metallic plate. It can be seen that the distillator with

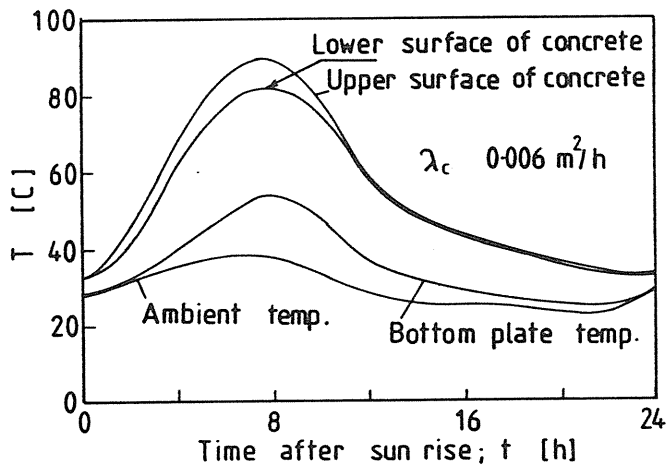


Fig. 2. 10. Variation of temperature with the operation time at upper slab surface, lower slab surface, bottom plate temperature and ambient temperature.

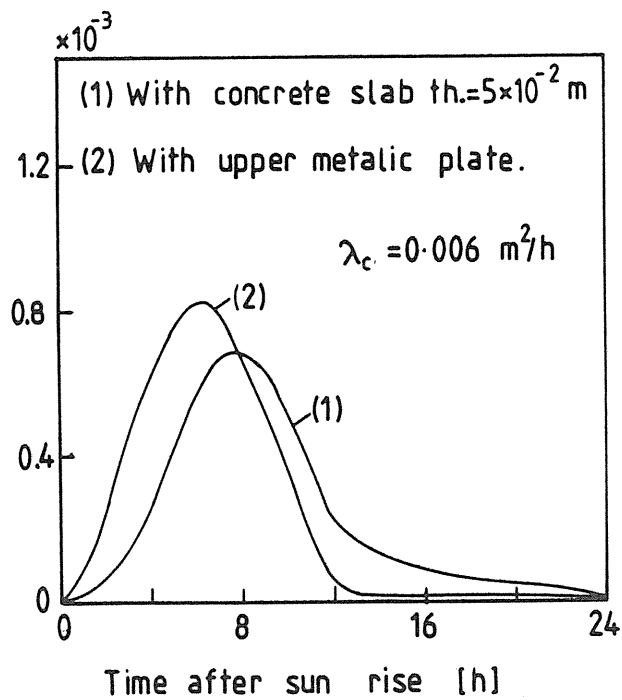


Fig. 2. 11. Variation of the distillate production rate with the operation time.

Table 2. 5. Operation conditions for maximum distillate with concrete slab and in Sept. at certain location at Red Sea in Egypt.

thickness (m)	t_1 (h)	t_2 (h)	F_1	F_2 (kg/h)	F_3	λ_c (m ² /h)
0.02	3	12	2.2	5.8	1.8	0.006
0.03	3	12	2.0	5.8	1.8	0.006
0.04	3	12	2.0	5.4	1.8	0.006
0.05	3	12	2.0	5.2	1.2	0.006

concrete slab has distillate during night operation due to the thermal storage.

Effects of the slab thickness and the thermal properties on distillate productivities were estimated and the result is shown in Fig. 2. 12. It can be seen that the use of sea water durable concrete results in only maximum 6 % decrease in the performance.

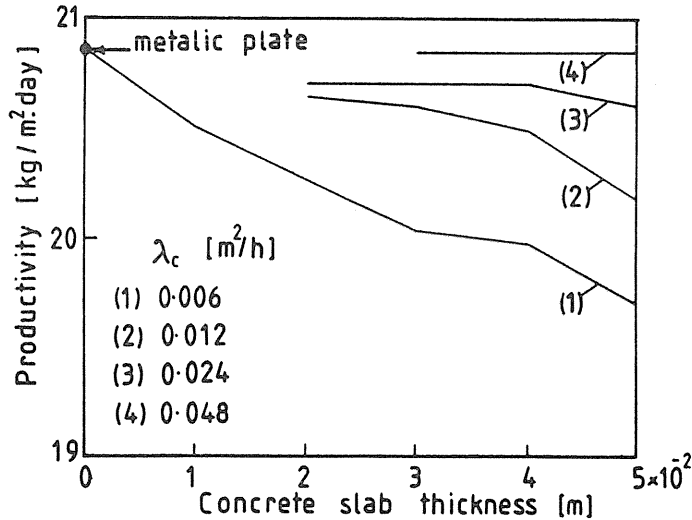


Fig. 2. 12. Effect of concrete slab thickness and thermal properties on distillate productivity.

2. 5. Conclusion

A dynamic model for multistage thermal diffusion type solar distillator was provided. The calculated results obtained by the model showed sufficient agreement with the data taken from both a laboratory test plant having 5 stages with 1 m² and a field test plant having 10 stages with 3 m² in frame area. The performance of distillator on four sample days through the year at certain location near Red Sea in Egypt was considered. The results at four sample days through the year showed that 5 stages distillator can give about 7 times the productivity of a conventional solar basin if the brine feed optimally scheduled.

The results showed that increasing parameters such as ambient temperature, sea water temperature and solar radiation improved the performance of solar distillator. The

sensitivities of the parameters which are controlling the distillate productivity solar distillator safe from thermal stresses and has high durability to hot sea water, the upper plate can be replaced with commercial concrete slab with maximum decrease in distillate productivity about 6 % for 5 cm slab thickness.

3. Laboratory Test of Solar Distillator with a Heat Penetrating Plate Having a Bend

3.1. Introduction

Solar distillators with wick attached behind the heat penetrating plate have been said to be promising^{3,4,5,10,11)} since the type is feasible to compose multistage and permits simple foundation. However, a sophisticated idea is required in the feeding system of liquid to the wick. Namely, capillary flow through the wick is sometimes difficult to compensate drying due to evaporation. Drying causes deposition of salt at the surface of wick to give a vital damage in the operation. Thus, keeping film flow over the surface of wick is necessitated for preventing the drying, but there is a difficulty to form stable liquid film extensively over the flat plate. Moreover, the heat penetrating plate is subjected to thermal expansion.

Hence, an idea to overcome them was proposed.¹²⁾ The heat penetrating plate of this invention is bended at the center line and has a channel for liquid flow below the crease of bending. The purpose of this study is to verify the idea by an experiment under cold conditions and to investigate the practical feasibility by a process simulation.

3.2. Experiment

The experimental apparatus is shown in Fig. 3. 1. The flat plate with a bend at the center line ③ was made from aluminum and was 450 mm long and 160 mm wide in one side. A fibrous sheet having thickness 1.3 mm, permeability $16 \times 10^{-12} \text{ m}^2$ and porosity 0.85 was attached below the plate as the wick and the zigzag end was lapped from the plate. A tube

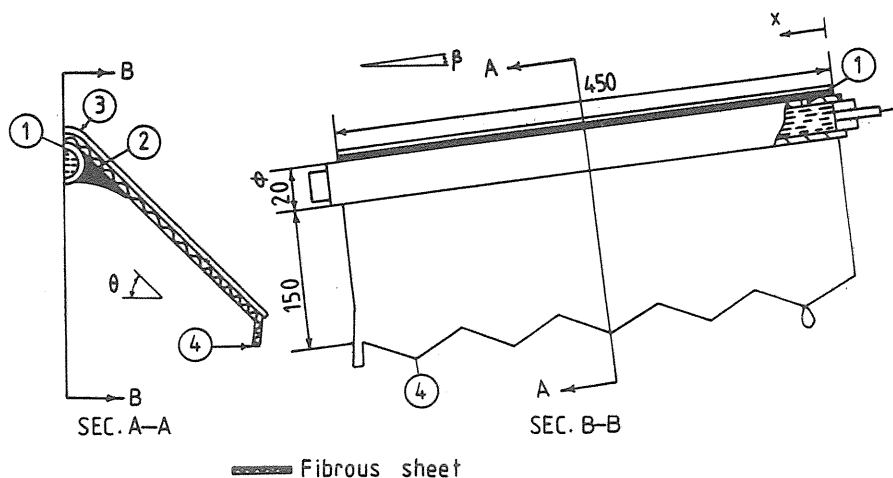


Fig. 3. 1. Experimental apparatus; 1-tube, 2-fibrous sheet, 3-aluminium plate, 4-zigzag laps.

of 20 mm in outer diameter was installed below the crease of bending as the liquid flow channel. Water was fed to the tube and was flooded from two holes near the inlet of the tube and then formed a meniscus between the outer surface of the tube and the fibrous sheet. This meniscus extended along the tube and part of the flow was delivered to the fibrous sheet. The dual holes were for manipulating the balance of water flow to both wings of the plate. The design was allowed for adjustment of the side angle θ and inclination β . The discharge rate from each lap of zigzag end was independently measured by periodical sampling. The meniscus flow along the tube was absorbed by capillary suction of a wrapped gauze at the projected end of the tube and the dipping rate from it was measured by also periodical sampling. The feed rate of water was changed from 0 to 5 kg/h · m and angles θ and β were respectively (41°, 43°) and (10°, 5°).

3. 3. Experimental Results and Discussion

Discharge rates measured from zigzag laps, the end side and meniscus flow along the tube are shown in Figs. 3. 2 and 3. 3. Where, the discharge rate from the end side was the amount collected from a triangle formed by the lower end of the plate, part of the bended crease and the gravity vector of the flow passing through the lower corner of the plate. The sudden rise of this discharge rate at a high flow rate was an end effect of the meniscus flow.

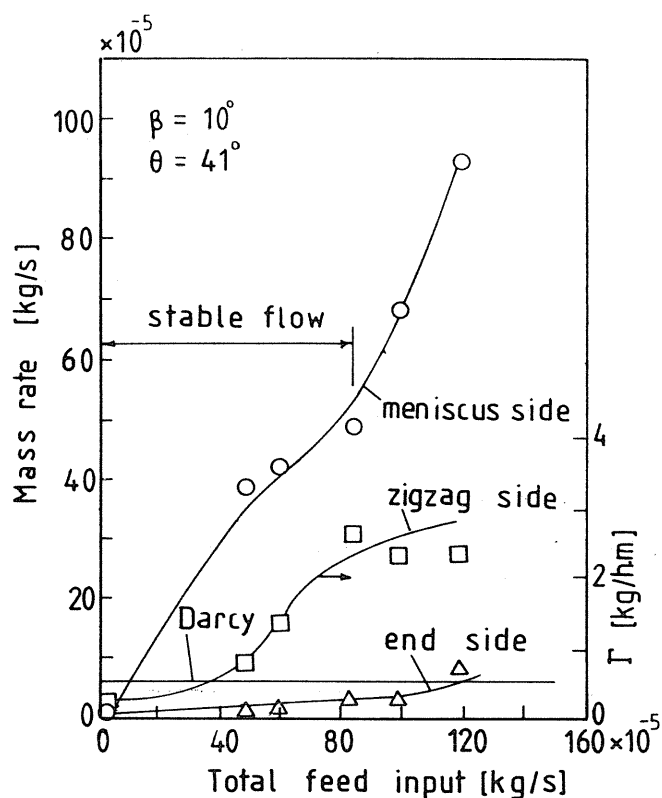


Fig. 3. 2. Discharge rates at $\beta = 10^\circ$ and $\theta = 41^\circ$.

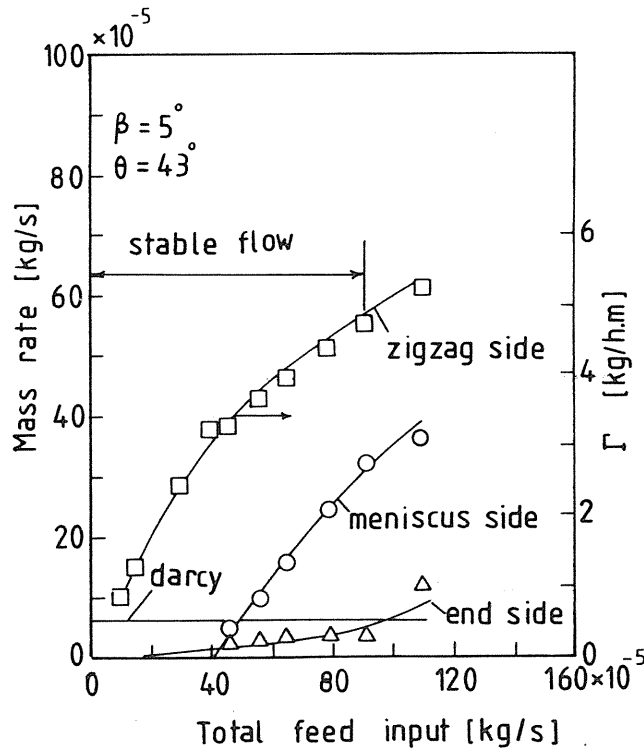


Fig. 3. 3. Discharge rates at $\beta = 5^\circ$, $\theta = 43^\circ$.

This discharge rate, however, can be out of consideration since the triangle will be eliminated if the axial inclination is fixed.

It was observed that Darcy flow controlled the flow in the fibrous sheet at a low feed rate and meniscus flow became higher than that from zigzag laps when the inclination angle was increased from 5 to 10 degree. In order to keep meniscus flow over all tube length, the feed rate must be higher than 0.4×10^{-3} kg/s for $\beta = 5^\circ$.

An uniform discharge from each zigzag lap is principally important for attaining uniform distillation over all solar heating area. This was verified by this experiment. A typical data are shown in Fig. 3. 4 which shows sufficiently uniform discharge. Such uniform discharge was attained in a range between 0.5 and 4.75 kg/h \cdot m at $\beta = 5^\circ$, $\theta = 43^\circ$ and between 0.5 and 2.6 kg/h \cdot m at $\beta = 10^\circ$, $\theta = 41^\circ$.

3. 4. Discussion on Availability to Practical Multistage Solar Distillator

As it is pointed out in the introduction, drying or deposition of salt at the surface of wick gives vital damage in the operation of practical solar distillator.

In order to predict a condition to avoid this, the equation to estimate film thickness is formulated as

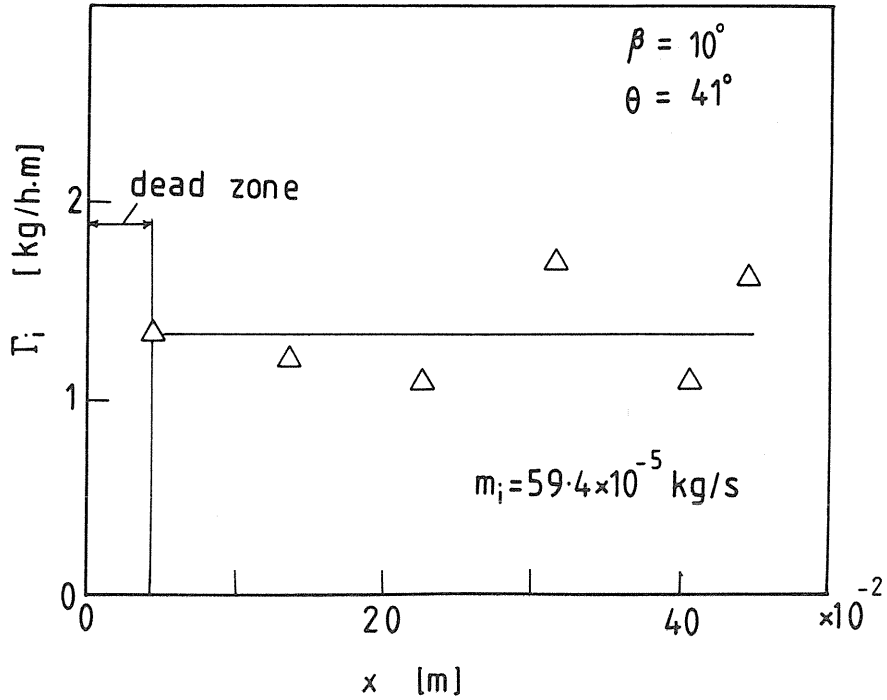


Fig. 3. 4. Discharge rate distribution along zigzag side at angle $\beta = 10^\circ$ and $\theta = 40^\circ$.

$$\rho_s \frac{\partial \delta}{\partial t} = -(\rho_s^2 g_{SP} / \mu_s) (K + \delta^2) \frac{\partial \delta}{\partial y} - h_m (P_s - P_D) \quad (1)$$

from mass and momentum balance where evaporation takes place from the surface.

The condition to control evaporation, i.e. P_s , P_D , and h_m are calculated in connection with process simulation of a multistage solar distillator which is extensively discussed in the paper simultaneously presented in this symposium.

Equation (1) was numerically calculated under the same condition to the presented paper. The results are shown in Figs. 3. 5 and 3. 6. Dimensionless film thickness at the outlet of the plate are plotted against time after sun rise for various feed rates as shown in Fig. 3. 5. No film thickness is appeared at the feed rate $\Gamma_i^* = 1.8$ kg/h·m and nearly 1 m of wing length in this case study. If normal sea water is assumed to be desalted, deposition of CaSO_4 will be another restriction in a practical operation. The concentration ratio of the outlet to the inlet is reciprocal of the dimensionless thickness if there was no diffusion of salt in the film flow. In this measure, Fig. 3. 5 also suggests that the critical feed rate will be 2.0 kg/h·m for nearly 1 m of wing length.

Meanwhile, the cold experiment here confirmed a preferable film flow in a range between 0.5 and 4.75 kg/h·m. Minimum film thickness distributions at $t = 6$ h are shown in

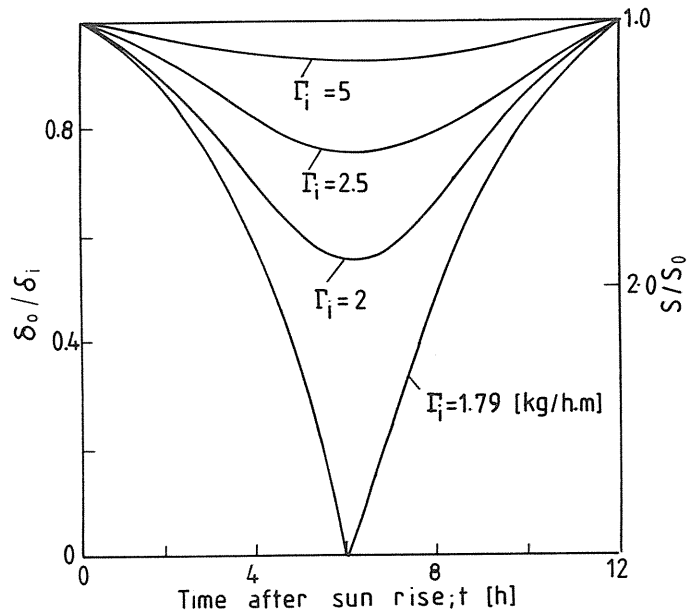


Fig. 3. 5. Outlet to inlet film thickness ratio vs. time for solar intensity $I_0 = 950 \sin(15t)$ at $\beta = 10^\circ$ and $\theta = 40^\circ$.

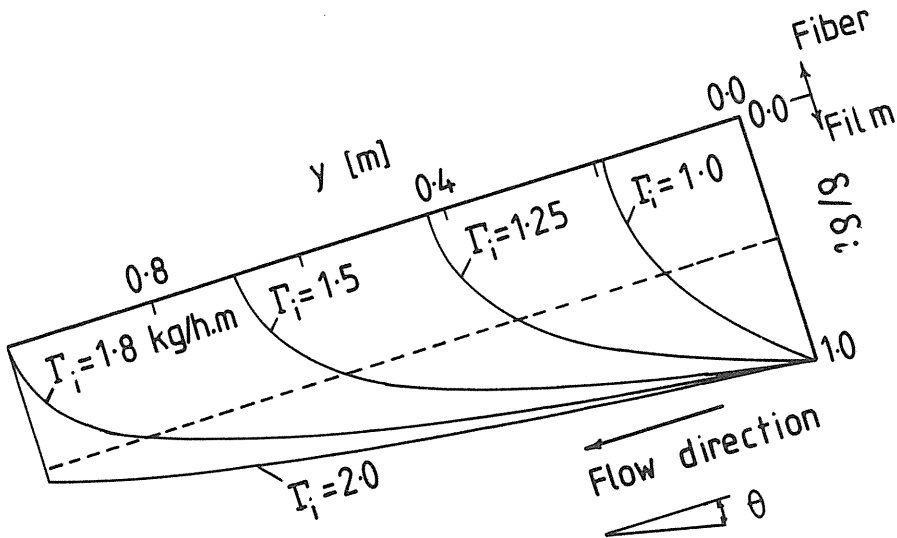


Fig. 3. 6. Film thickness distribution versus plate length in the direction of gravity at $\beta = 10^\circ$, $\theta = 40^\circ$ and solar intensity $I_0 = 950 \sin(15t)$.

Fig. 3. 6. The dotted line indicates an approximately restricted film thickness from scale deposition. The length crossing the line suggests the allowable dimension of the plate in the direction of gravity vector. This is the verification that the proposed idea is capable of applying to a solar distillator free from scale formation.

3. 5. Conclusion

A new idea of feeding mechanism was proposed and verified by a cold experiment. Theoretical calculations showed that this mechanism is enough to overcome drying of wick. The paper supplied data helpful for the application of this type.

4. Heat and Mass transfer during Evaporation from a Free Surface of Water Flowing through Fibrous Sheet in an Inclined Enclosure

4. 1. Introduction

A multistage thermal-diffusion solar still has been developed in Japan.³⁾ The authors have conducted a series of studies to support the project and have presented static⁴⁾ and dynamic⁵⁾ simulations of the process with a simplified mathematical model. However, heat and mass transfer in the still are not so simple if the phenomena are observed in detail. Its main part is composed of several enclosures of which the upper boundary is a fibrous sheet attached below a waterproof partition. Published works¹³⁾ related to thermal convection in such the enclosure have mostly dealt with isothermal wall conditions. Sparrow and Prakash¹⁴⁾ recently studied this phenomena simultaneously with internal and external convection at one side wall and it was found theoretically that the Nusselt numbers were about sixty percent of those for isothermal conditions.

The problem encountered here, however, is more complicated since the enclosure of the solar still also requires consideration of evaporation and condensation within it. Hence this study emphasized experiment and aimed to provide instructive data for the development of the new type of solar still.

4. 2. Experimental Apparatus and Procedure

Essential parts of the experimental apparatus are shown in Fig. 4. 1. The enclosure in which evaporation and condensation took place was 0.74 m long, 0.285 m wide and 0.02 m deep. Two kinds of fibrous sheet as described in Table 4-1 were respectively attached below the upper plate ⑬ of the enclosure to allow for liquid flow. The upper plate was made from aluminum and was heated from above by two main heaters ⑨. Each heater was assembly of stainless steel strips having a thickness of 0.1 mm. The main heater ⑨ was mounted on the upper plate ⑬ after inserting a thin mica sheet between them for electrical insulation and they were fixed by a frame.

Two sensors ⑪ to detect heat flux were installed at an intermediate plane above the main heaters. Two guard heaters ⑩ were placed above the main heaters. Power to each guard heater was individually adjusted to maintain the heat flux through the intermediate plane ⑩ at zero. Thus the electric power applied to the main heaters could be identical to the heat input to the upper plate and the heat loss from the side walls, detected by heat flux meters ⑫.

The lower boundary of the enclosure was a 1 mm thick aluminum plate 14 where condensation took place on the upper surface and heat was rejected from the lower surface to the atmosphere by radiation and natural convection. Two angles of inclination were used in

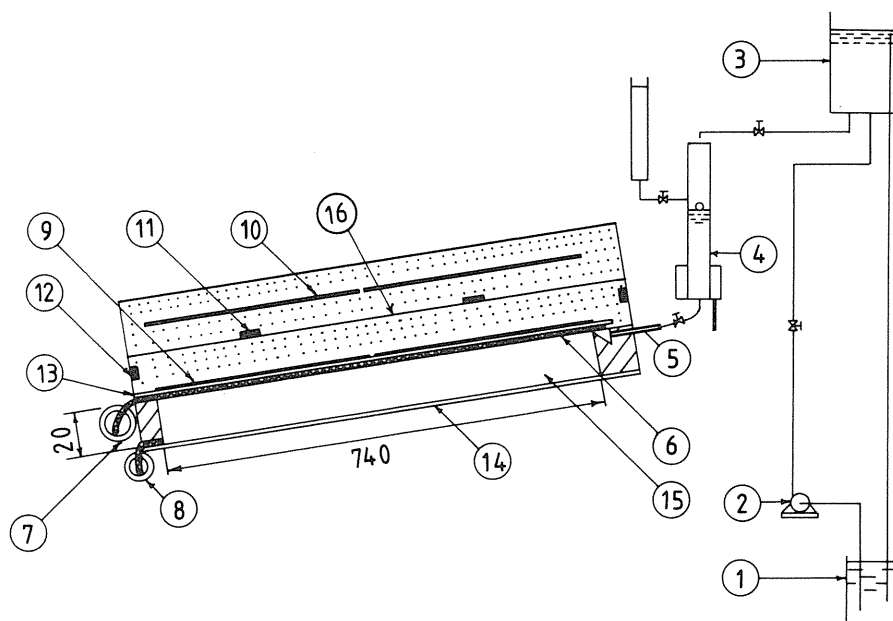


Fig. 4. 1. Experimental apparatus: 1-Tank; 2-Pump; 3-Constant-head tank; 4-Feed measuring system; 5-Feeders; 6-Fibrous sheet; 7-Outlet water drum; 8-Distillate drum; 9-Main heaters; 10-Guard heaters; 11-Sensors of heat flux meter; 12-Side loss heat flux sensors; 13-Upper plate; 14-Lower plate; 15-Enclosure; 16-Intermediate plane.

this study: 10 degrees to give a sufficient driving force for flow and 36 degrees for suitable reception of solar beams in Japan.¹⁵⁾ A sponge material was inserted at the inlet side of the fibrous sheet for uniform feeding of water. The feed rate of water was regulated and measured by a cylinder ④ in Fig. 4. 1.

The evaporation rate was determined by measuring the feed and discharge rates. The amount of distillate was also measured at long intervals for confirmation of the evaporation rate after attaining steady state.

Power to the main heaters was regulated to adjust the net heat flux to the upper plate to a set value. For one group of experiments the heat flux input was kept constant at 430 W/m^2 and the feed rate was changed from 0.43 to $3.8 \text{ kg/h} \cdot \text{m}$. For the second group the feed rate was kept constant at $1.17 \text{ kg/h} \cdot \text{m}$ and the heat flux input was changed from 117.5 to 430 W/m^2 .

Temperature distributions of the upper and the lower plates in the flow direction were measured respectively by 11 and 12 sets of copper constantan thermocouples attached to the upper surfaces of the plates along the center lines. The temperatures were recorded to determine the steady-state condition, which was attained after about 7 h from starting. Room temperature was controlled at $22.5 \pm 0.5^\circ \text{C}$ for all test runs.

4. 3. Results and Discussion

4. 3. 1. Temperature distribution

Curves shown in Fig. 4. 2 (a, b and c) are representative for those obtained from several runs with A and B sheets. In all cases the feed temperature of water was 22°C but a sudden rise was observed at the inlet due to the high conductivity of the aluminum plate attached to the fibrous sheet, as will be discussed later. The preheating zone is defined here as the distance from the inlet to the point of maximum temperature. A slight decrease in temperature was observed near the outlet, and this tendency becomes clear with decreasing feed rate. This

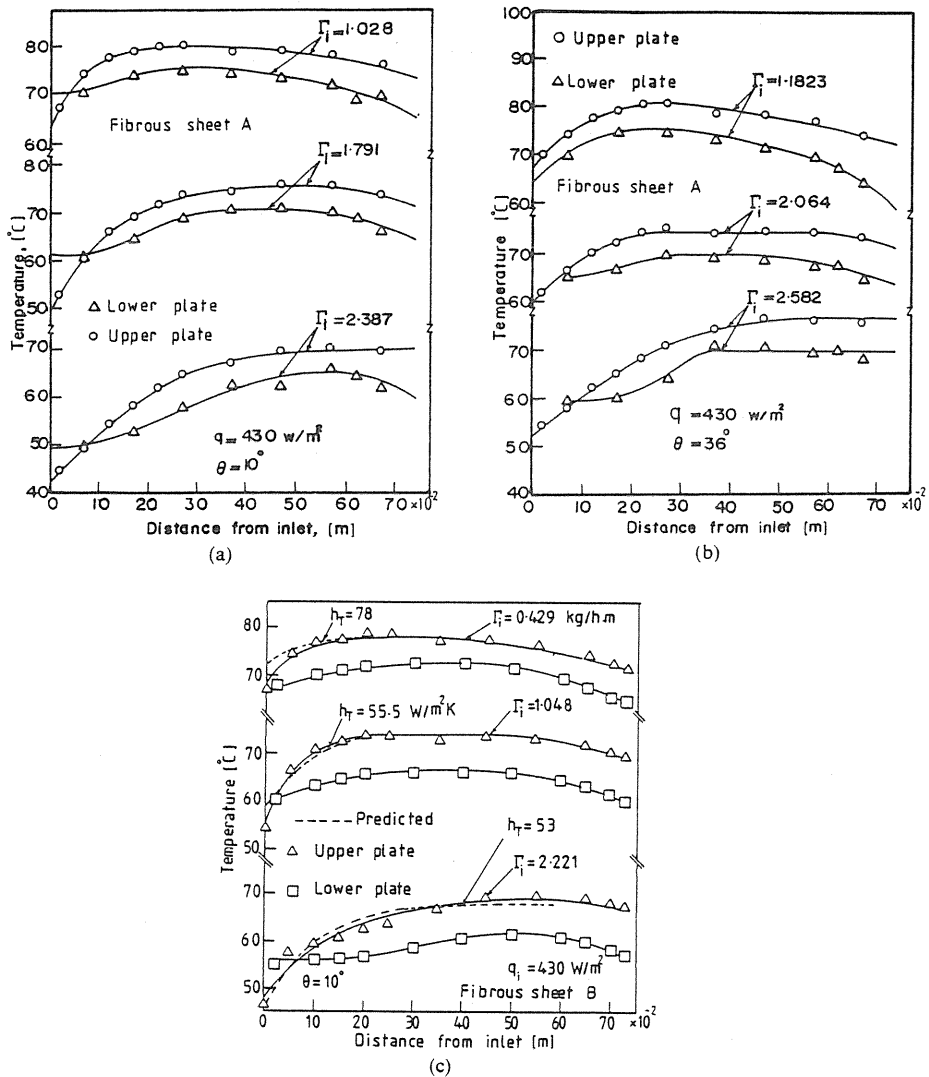


Fig. 4. 2. Temperature distributions for both the upper and lower plates in direction of flow for different feed rates Γ_i (kg/h · m).

could be attributed to thermal convection near the outlet side of the enclosure, as will be discussed in Section (4. 3. 2). A crossing of two curves at the inlet was observed in some cases and this suggests that condensation of vapor takes place even at the upper sheet and results in rapid heating there. Temperatures at the lower plate for type B sheet were more uniform than those for type A. For both types it became more uniform with decreasing feed rate.

The maximum temperature at the upper plate was dependent on the heat flux and was almost independent of the feed rate and the kind of fibrous sheet, as shown in Fig. 4. 2 (a, b and c). This tendency is described in Fig. 4. 3, which gives the empirical equation.

$$T_{max} = 0.1q_i + 31.0 \quad (1)$$

This equation is valid for the range between 117.5 to 430 W/m.²

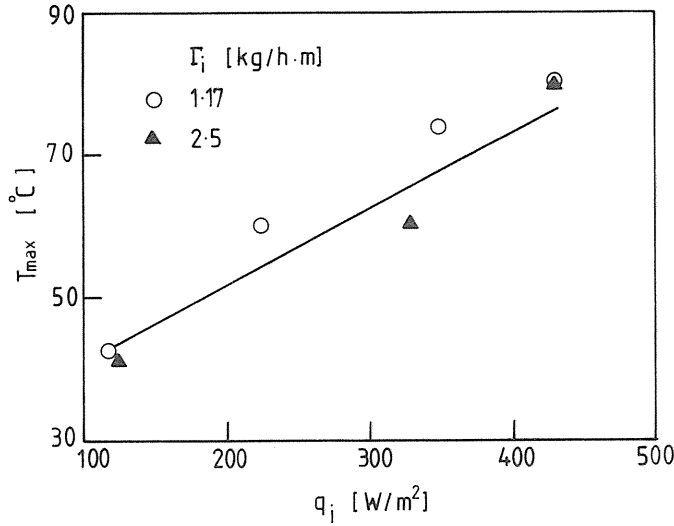


Fig. 4. 3. Maximum upper plate temperature vs. heat flux.

4. 3. 2. Heat and mass transfer

Heat supplied to the upper plate was consumed in evaporating liquid Q_{ev} , rising enthalpy of water Q_{fl} , heat convection Q_{co} , and heat radiation from the evaporating surface Q_r . These balance equations are given by:

$$Q_i = I_E - Q_{sl} \quad (2)$$

$$Q_{fl} = m_o C_{pwo} T_o - m_i C_{pwi} T_i \quad (3)$$

$$Q_i - Q_{fl} = \varepsilon k_w A_{es} (T_p - T_{es}) / \delta \quad (4)$$

$$Q_{ev} = m_{ev} \lambda \quad (5)$$

$$Q_r = \sigma \varepsilon' A_{es} [(T_{es} + 273.15)^4 - (T_C + 273.15)^4] \quad (6)$$

$$Q_{co} = Q_i - (Q_{fl} + Q_{ev} + Q_r) \quad (7)$$

Where, I_E , Q_{sl} , T_P , m_o , and m_i were measurable. The physical properties in the mathematical equations are given in Table 4. 1.

Table 4. 1. Physical properties and constants.

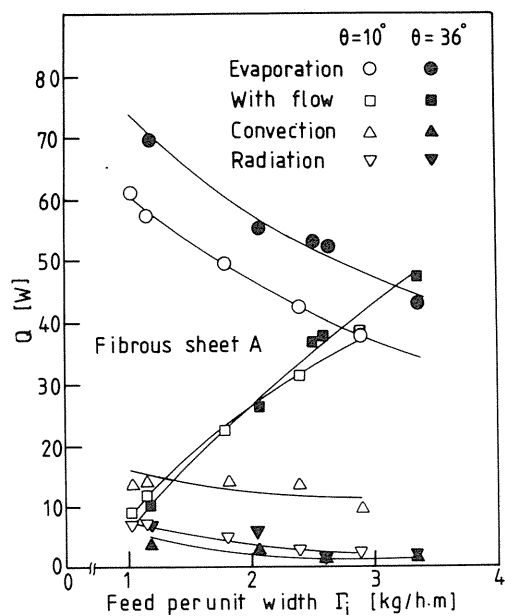
Physical properties of fibrous sheets:	
Type A	
$\varepsilon = 0.95$	$[-]$
$K = 2.435 \times 10^{-10}$	$[m^2]$
$\delta = 1.6 \times 10^{-3}$	$[m]$
Type B	
$\varepsilon = 0.85$	$[-]$
$K = 6.4 \times 10^{-11}$	$[m^2]$
$\delta = 1.3 \times 10^{-3}$	$[m]$
Viscosity of water:	
$\mu_w = \exp[571.893/(T + 133.15) - 10.6399]$	$[kg/s \cdot m]$
Thermal Conductivity of Water:	
$k_w = 0.4768 T^{0.074}$	$[W/m \cdot K]$
Latent heat of water:	
$\lambda = 2325.59 \times 10^3 \{1072.653 - 1.0166 T_{es} + 1.4087 \times 10^{-4} T_{es}^2 - 5.146 \times 10^{-6} T_{es}^3\}$	$[J/kg]$
Vapor pressure of water:	
$p = 133.32 \exp\{18.6686 - 4030.1824/(T + 235)\}$	$[N/m^2]$
Gas constant of vapor:	
$R_v = 461.88$	$[J/kg \cdot K]$
Density of vapor:	
$\rho_v = p/(R_v, T)$	$[kg \cdot m^3]$
where T is in Kelvin	

Then each heat flux could be determined from these equations. The calculated results are shown in Fig. 4. 4. It indicates that convection in the enclosure decreases with increasing inclination. This is attributed to the promotion of natural convection at the external cooling surface of the condensating plate, which results in fewer temperature variations in the flow direction.

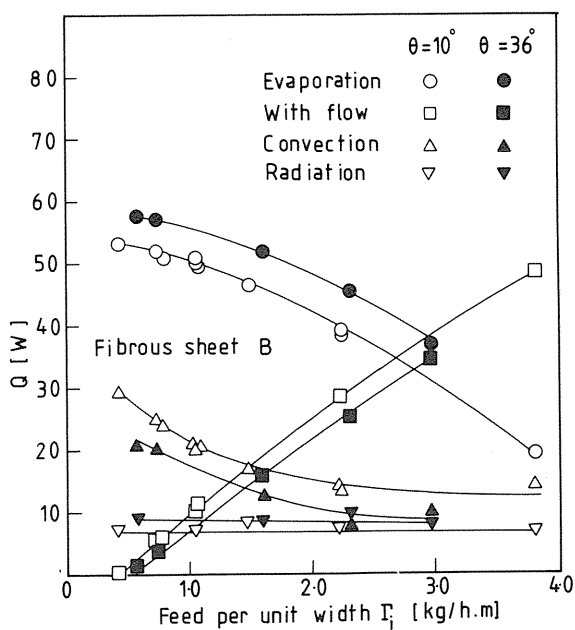
The term $q_{co}/(\Delta T)_{av}$ can be used as a parameter of heat transfer to study the inside convection, where the average temperature difference $(\Delta T)_{av}$ is given by

$$(\Delta T)_{av} = \frac{1}{L} \int_0^L (T_{es} - T_C) dx \quad (8)$$

The values are shown in Fig. 4. 5, where the dotted line indicates the contribution of thermal conduction through the stationary gas layer. The evident increase at lower feed rates



(a)



(b)

Fig. 4. 4. Heat breakdown of thermal flow for both kinds of fibrous sheet.

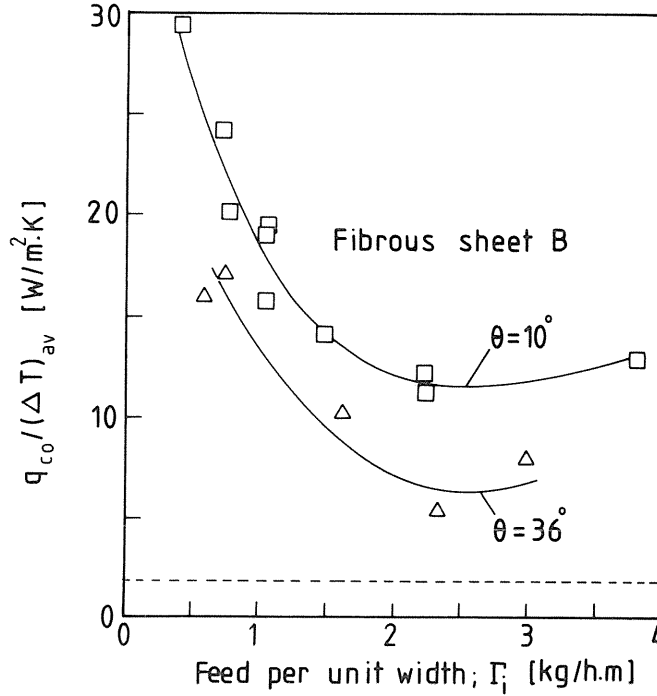


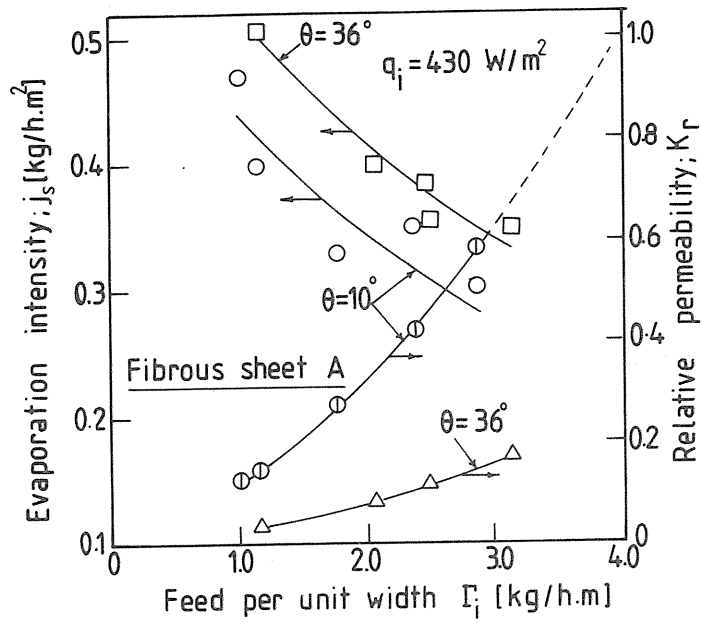
Fig. 4. 5. Convection parameter $q_{co}/(\Delta T)_{av}$ for various feed rates.

is interpreted to mean that the higher evaporation intensity due to higher temperature levels promotes displacement of the gas mixture. The slight increase in the parameter $q_{co}/(\Delta T)_{av}$ at higher feed rates can be attributed to the large temperature gradient in the flow direction as shown in Figs. 4. 2 (a, b, and c).

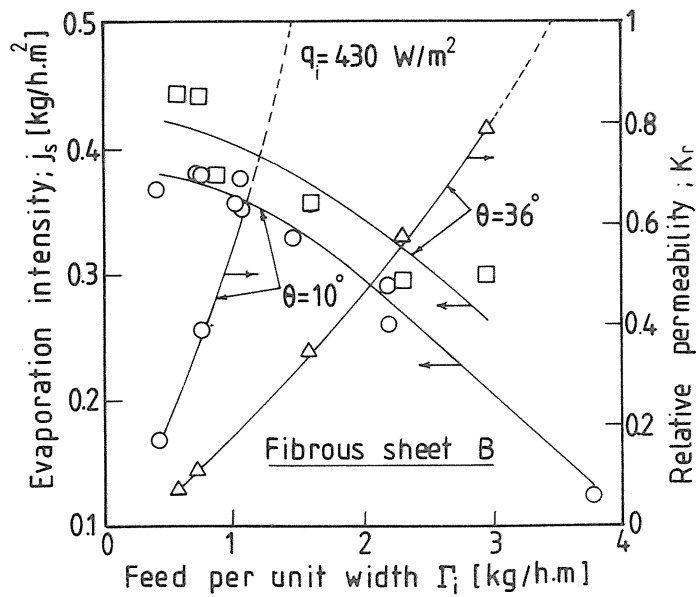
When evaporation takes place, the fibrous sheet reaches an unsaturated condition (drying from the surface). Hence the condition at the outlet was calculated and is shown in Fig. 4. 6 together with evaporation intensities for various feed rates. Relative permeability K_r is given by

$$K_r = \frac{\Gamma \cdot \mu_w}{K \rho_w (\rho_w - \rho_v) \cdot g_x \delta} \quad (9)$$

This is the ratio of the permeability of the fibrous sheet to that of the saturated condition defined by Darcy's equation under an assumption of $\delta \ll L$. The intersection at $K_r = 1$ in these figures gives the feed rate at which saturation takes place and film flow would appear at higher flow rate, namely $\Gamma_i > 1.5 \text{ kg/h} \cdot \text{m}$ for $\theta = 10$ degrees and $\Gamma_i > 3.5 \text{ kg/h} \cdot \text{m}$ for $\theta = 36$ degrees with type B fiber. This condition is preferable for preventing deposition of salt in operating solar stills. The average film thickness at $\Gamma = 3.8 \text{ kg/h} \cdot \text{m}$ and $\theta = 10$ degrees with type B fiber is estimated to be 80 microns by Nusselt's equation. Operations at a 36 degree angle produce more distillate than that at a 10 degree angle for both kinds of fibrous sheets, but unsaturation is always presumed.



(a)



(b)

Fig. 4. 6. Evaporation intensity $j_s(\text{kg/h}\cdot\text{m}^2)$ and relative permeability (K_r) vs. feed rate for both kinds of sheets and two inclinations.

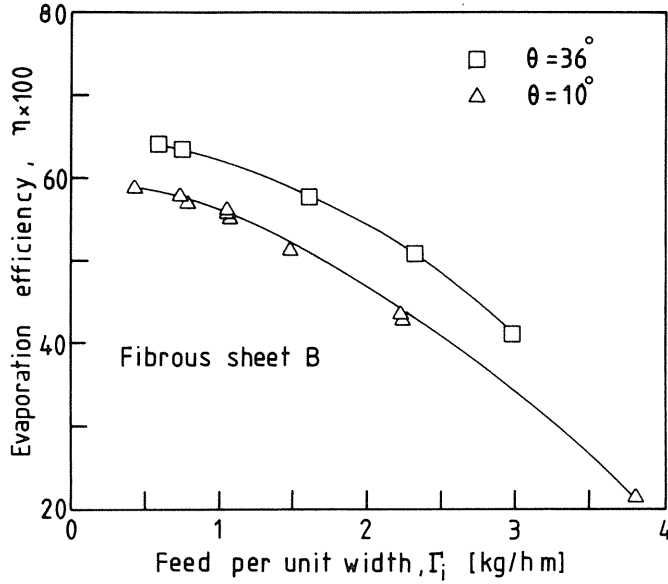


Fig. 4. 7. Evaporation efficiency η vs. feed rate for sheet B and different inclinations.

Evaporation efficiency is defined as the ratio of the heat consumed in evaporation to the heat supplied to the upper plate. The experimental data are shown in Fig. 4. 7. The value reached a maximum of 64 % and decreased with increasing feed rate due to the loss of sensible heat.

4. 4. Analysis of Temperature Distribution

Temperature distributions in the direction of flow and the length of enclosure required for preheating are of essential importance in designing a practical apparatus.

The internal thermal resistance through the thickness of the upper aluminum plate could be neglected, and the temperature difference between the two sides of the fibrous sheet was estimated to be less than 0.9°C. Therefore, one dimensional and one representative temperature model for both the fibrous sheet and the aluminum plate could be applied to the study of temperature distributions in the preheating zone.

Then the energy balance equation is given by

$$K_T \frac{d^2 T_P}{dx^2} - \Gamma_i C_{pw} \frac{dT_P}{dx} - h_T (T_P - T_C) + q_i = 0 \quad (10)$$

where

$$K_T = k_{al} \delta_{al} + \varepsilon k_w \delta \quad (11)$$

The boundary conditions are given by

$$x = 0 ; \quad K_T \frac{dT_P}{dx} = \Gamma_i C_{pw} (T_P - T_{wi}) \quad (12)$$

$$x = x_{fd} ; \quad \frac{dT_P}{dx} = 0 \quad (13)$$

The total heat transfer coefficient²⁾ h_T is composed of not only convection and radiation but also evaporation, which is defined by

$$h_{ev} = \frac{q_{ev}}{(T_P - T_C)} \quad (14)$$

There preheating length x_{fd} was determined by computer from the experimental curve, and the temperature distributions were calculated by changing the total heat transfer coefficient, h_T , until it fitted the experimental data. Dotted lines in Fig. 4. 2(c) indicate calculated curves and the total heat transfer coefficient obtained by the convergence is plotted against the feed rate together with preheating length x_{fd} as shown in Fig. 4. 8. The values of h_T in Fig. 4. 8 shown the same tendency as the convection parameter in Fig. 4. 5. The values of h_T for 36 degree inclination are lower then for 10 degree inclination although evaporation in the first case is high. This means that the convective heat transfer coefficient is the most dominant component in h_T at the preheating zone.

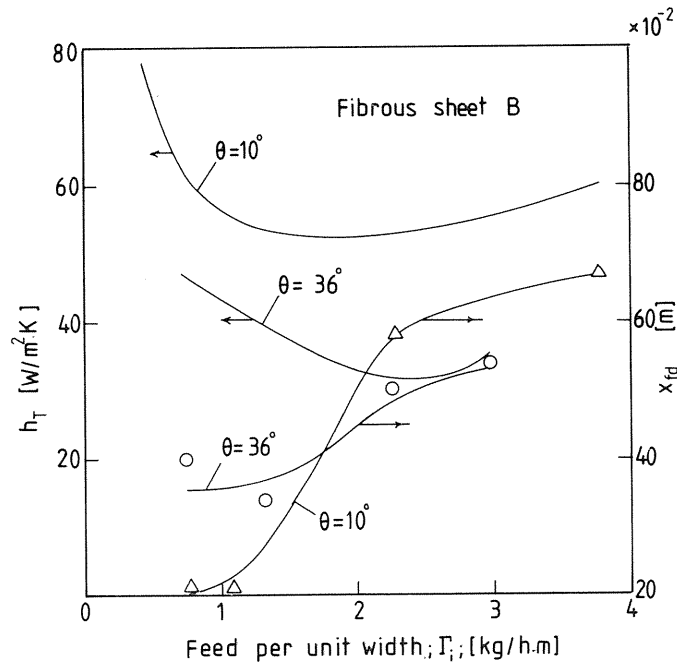


Fig. 4. 8. Total heat transfer coefficient from evaporation surface to lower plate together with x_{fd} against feed rate in the preheating zone.

4. 5. Conclusion

Thermal behavior of an enclosure composed of an upper evaporation (heating) plate and a lower condensing plate were studied as a fundamental work for developing a new type of solar still, and the following points were revealed:

Evenness of temperature distribution in the flow direction of liquid is attained when the liquid flow is lower and a less-permeable fibrous sheet is attached below the upper plate.

The maximum temperature of the fibrous sheet was almost independent of kind of fiber and feed rate, and its value was linearly proportional to the heat input.

Operation at a 36 degree angle gave about 20 % rise in evaporation rate for A type fibrous sheet as compared with that at 10 degree and 12 % for B type at ($\Gamma_i = 1 \text{ kg/h} \cdot \text{m}$). Type A fibrous sheet gave about 16 % rise in evaporation rate at a 10 degree angle and 30 % at a 36 degree angle compared with B type. When using B type fibrous sheet at a 10 degree angle, the feeding liquid forms film flow, which is the preferable condition for the solar still.

Thermal convection inside the enclosure was intensive at lower feed rates and was nearly constant at higher feed rates.

Temperature distributions at the upper plate were analysed and revealed that convective heat transfer was the most dominant in the preheating zone.

5. Development and Application of a Roof Type Solar Still

5. 1. Introduction

An extensive study has been conducted to develop a roof type solar still with wick attached behind the heat penetrating plate which is feasible to compose multistage and permits simple foundation.^{4,10,16,17)} A key technology for trouble free operation of this type of still is to form stable liquid film flow below the surface of wick. Hence, an sophisticated idea was provided, that is, the heat penetrating plate is bended at the center line and has a channel for liquid flow below the crease of bending. A test under cold conditions has proved the idea to be feasible.¹⁸⁾

This section deals with the result obtained under heating conditions with a test apparatus mainly made from polyethylene film and also discusses the application to a hybrid system combined with a panel of photoelectric cell which is substituted for the heat receiving plate.

5. 2. Experimental Apparatus

The experimental apparatus of two stage still is shown in Fig. 5. 1. Bags of 500 mm^2 square were made from polyethylene film of 1 mm in thickness. Each of them was penetrated by a tube of 15 mm in diameter at the center and bended by stretching both sides at an arbitrarily given angle. Fibrous sheets of 1.3 mm in thickness as wick was attached inside of the upper film of the bag. The diffusion gap was supported at 15 mm by the central round tube and rectangular pipes at both sides. Two such bags were filed and aluminum plate was placed on the upper surface to receive heat.

Salt water was fed to the central tube from a head tank and was flooded from two holes near the inlet of the tube and then formed a meniscus between the outer surface of the tube and the fibrous sheet. This meniscus extended along the tube and the most of salt water was filmwisely flowed along direction of the gravity vector below the fibrous sheet. The dual holes were for manipulating the balance of liquid flow to both wings of the sheet. The side angle and the inclination angle were respectively fixed at 14.6° and 9.7° . Concentration of the salt water was 1 % in NaCl wt % to trace bypathing and leakage, and feed rate was changed from 0.7 to $1.0 \text{ g/m}^2 \cdot \text{s}$.

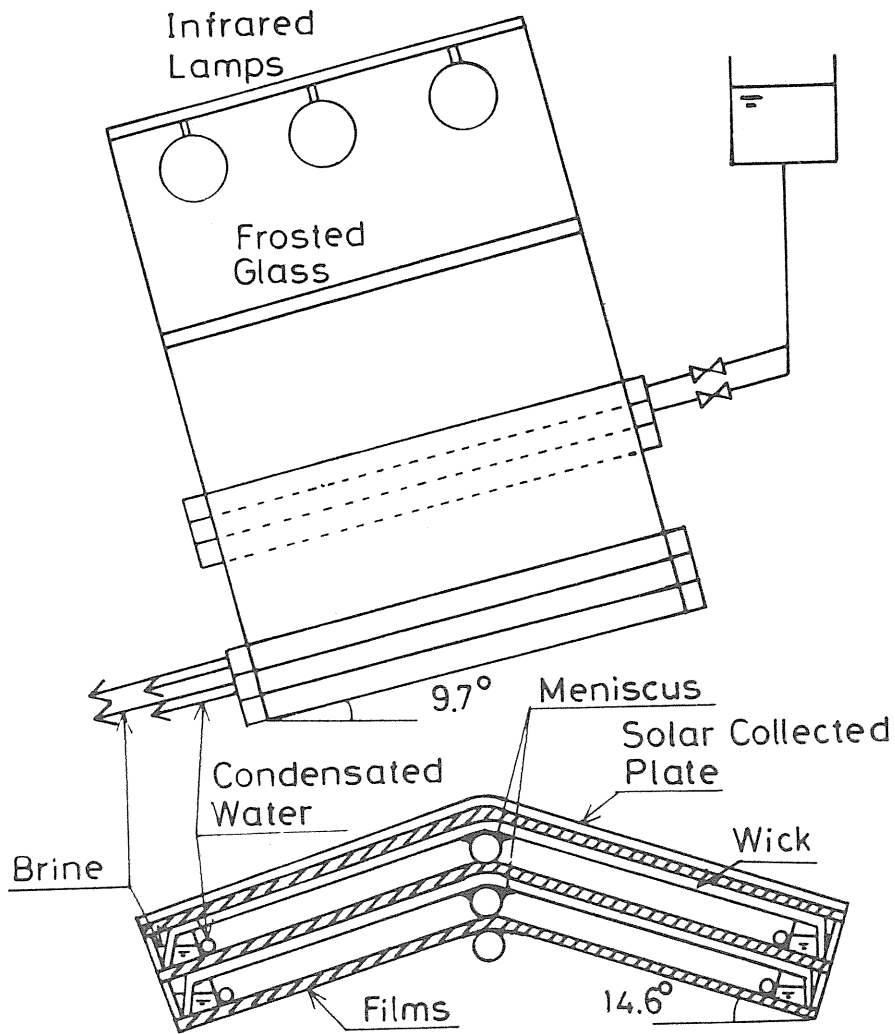


Fig. 5. 1. Experimental apparatus.

The upper plate of the test still was heated by infrared lamps through two sheets of frosted glass to attain uniform irradiation. The intensity was from 240 to 650 W/m. Then, a portion of salt water was evaporated from the surface of fibrous sheet by receiving heat from the upper plate and condensed above the opposite surface. The condensed fresh water (product) was assemble to rectangular tubes at the both sides. The latent heat of condensation transfered through the film of the second stage and heated salt water fed to the second stage. Thus, two effect of evaporation was performed.

Copper constantan thermocouples were installed respectively at four points along the flow direction for measuring temperature distributions of a plate to receive irradiation, salt water and distilled water. Flow rate of feed salt water, distilled fresh water and discharged condensate were determined by measuring weights, and their salt concentration were also determined by measuring by electric conductivity.

5. 3. Experimental Result and Discussion

Temperature distributions of heat receiving surface, evaporating liquid and condensed fresh water are shown in Fig. 5. 2 for two irradiation intensities, where temperatures at symmetrical positions of both roof wings were arithmetically averaged. They also indicate that temperature distributions along the tube direction could be considered to be uniform.

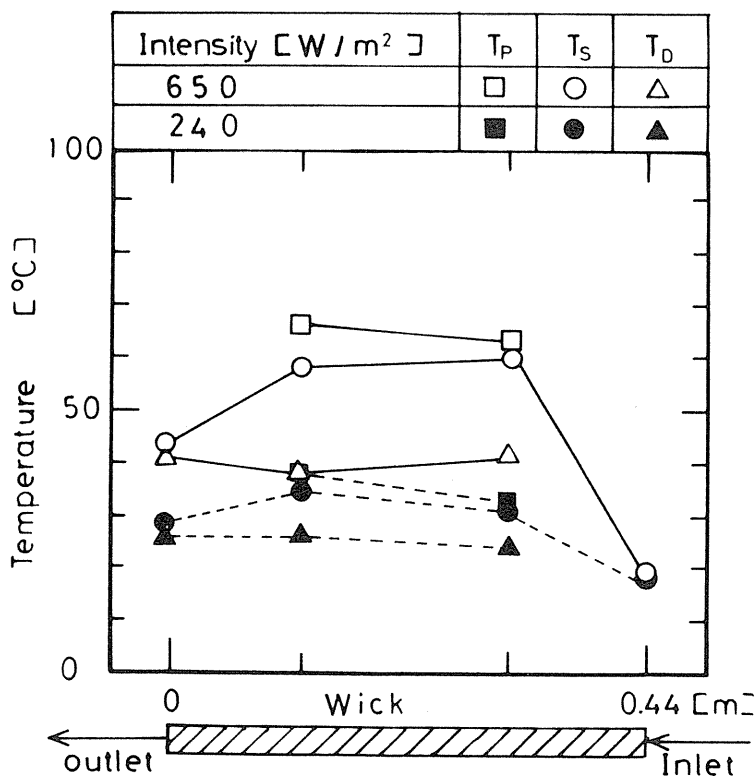


Fig. 5. 2. Temperature distribution.

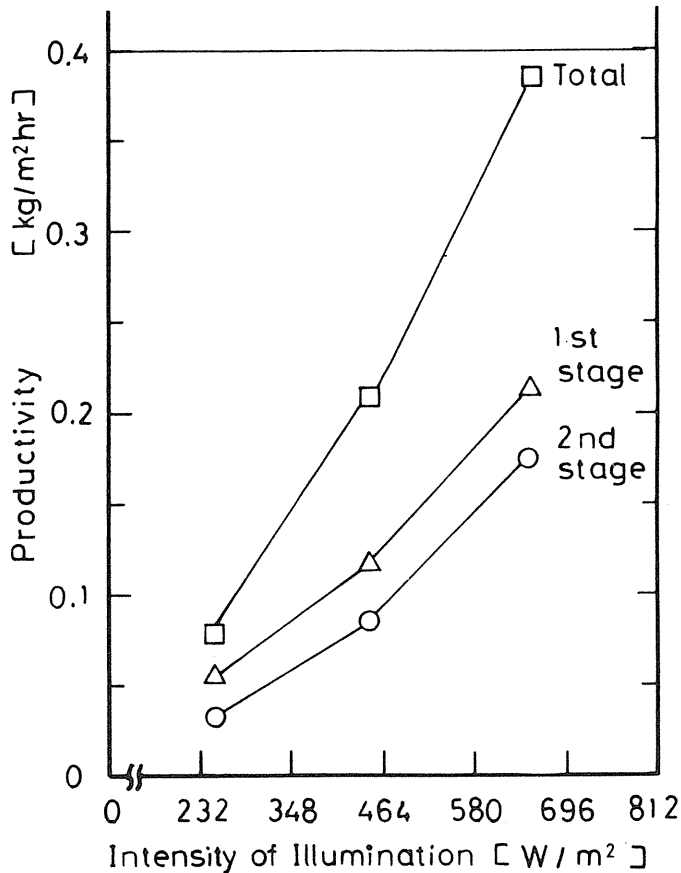


Fig. 5. 3. Productivity.

Fresh water productivities are plotted against irradiation intensity as shown in Fig. 5. 3. Salt concentrations of condensed fresh water were all less than 1 ppm. The concentration of supplied liquid was 0.1 NaCl wt % which was 1/35 standard salinity of sea water. Then, if it tested by sea water, maximum salinity of produced fresh water will be at 35 ppm which satisfactorily clears the standard of drinking water.

When evaporation takes place at the surface of the fibrous sheet, the thickness of film flow will be decreased and deposition of sodium sublimate is predicted where the thickness is diminished to half in normal desalination of sea water. If the film flow is disappear, it means the surface of fibrous sheet is dried. These conditions were extensively discussed in the previous paper.¹⁶⁾ The experiment in this study was carried out within the restriction, and succeeded to produce fresh water and proves the proposed system to be feasible.

5. 4. A Hybrid System of Solar Still Combined with Photo Cell Panel

Metallic materials would not be suitable to constructing solar stills with such low productivity. Copper-Nickel alloys have been widely used for the tube material in multistage flash evaporators. While, if Cu-Ni was selected, the cost of heat transfer tube forms 30 ~ 50 % of

total construction cost of the evaporator. Sea water fed to such evaporators is usually heated above 100°C and pretreated for protecting against corrosion and scale formation. Many sophisticated pretreatment process have continuously developed, and no sufficient material has still been found. Solar stills would not permit any sophisticated pretreatment process since it requests simple operation. Productivity of fresh water per heat transfer area for solar stills is briefly $1/300$ that for multistage flash evaporators. It becomes now obvious that any metallic material is unsuitable to constructing solar stills.

With this concept, use of concrete slab for the upper plate to receive solar irradiation was studied by computer simulation, and revealed the advantage.¹⁶⁾ The bended roof type solar still tested in this study was made from plastic film from this view point. The design will request no firm ground construction and permit to be foldable. Then, such the still can be portable use like a tent if sea water is fed from a head tank which is capable of daily supply. This design is expected to favorably use in caravan, resource survey and military front.

Stable operation was succeeded by the indoor laboratory test. However, if such film made still is attacked by strong wind, the still will be vibrated to break stable film flow at the fibrous sheet and salt water will contaminate the distilled fresh water unless any guard against the wind is installed.

From this view point, a hybrid system of such roof type solar still combined with photoelectric cell is proposed. The concept is to substitute the photo cell panel for the roof plate of solar still below which is attached by fibrous sheet to permit flow of salt water to extract fresh water. The design allows to eliminate the cost of roof to receive solar irradiation which forms major part of the construction cost. The function of evaporator is also advantageous to cool the photo cell since the out put of photo cell is increase approximately 0.5% with decrease of temperature in every one degree centigrade.

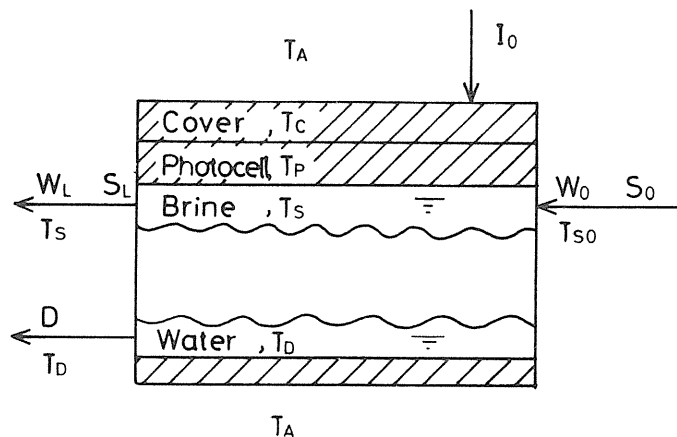


Fig. 5. 4. Heat & mass flow.

The flow of mass and heat of such hybrid system is shown in Fig. 5. 4. The system is consisted of a glass cover, a photo cell panel and a single stage solar still. Mass and heat balance equations for respective parts are described as follows under an assumption that temperature distributions along the axial direction are uniform.

Cover:

$$\rho_C L_C C_C \frac{dT_C}{dt} = \alpha_C I_0 + U_{PC} (T_P - T_C) - H_{CA} (T_C - T_A) - \sigma \epsilon_{CS} F_{CS} (T_C^4 - T_{sky}^4) \quad (1)$$

Plate:

$$\rho_P L_P C_P \frac{dT_P}{dt} = \alpha_P \tau_C I_0 - U_{PC} (T_P - T_C) - U_S (T_P - T_S) \quad (2)$$

Brine:

$$\begin{aligned} \rho_S L_S C_S \frac{dT_S}{dt} = & H_{S0} W_0 + U_{PS} (T_P - T_S) - H_S W_L - H_D D \\ & - R_S D - (k/z) (T_S - B - T_D) \\ & - \sigma \epsilon_{SD} F_{SD} (T_S^4 - T_D^4) \end{aligned} \quad (3)$$

Water:

$$\begin{aligned} \rho_D L_D C_D \frac{dT_D}{dt} = & R_D D + (k/z) (T_S - B - T_D) \\ & + \sigma \epsilon_{SD} F_{SD} (T_S^4 - T_D^4) - U_{DA} (T_D - T_A) \end{aligned} \quad (4)$$

$$D = \frac{D}{ZA} \frac{(T_S - P_D)}{P_{BM}} \quad (5)$$

Physical properties and constant substituted in the calculation were identical to the reference.⁴⁾ A set simultaneous ordinary differential equations (1) ~ (4) was solved by Runge-Kutta method. Calculated photo cell temperatures and fresh water productivity are plotted against solar intensity as shown in Fig. 5. 5.

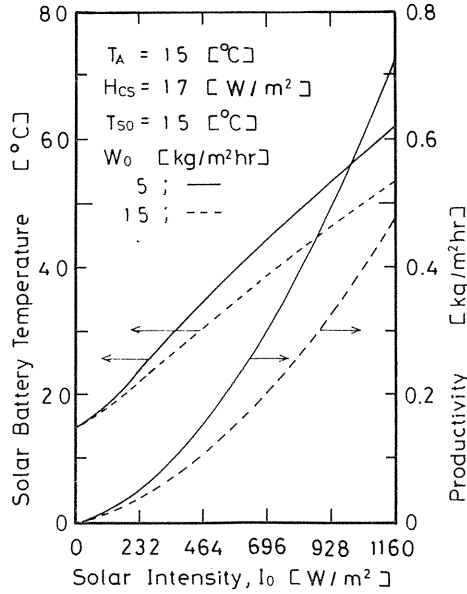


Fig. 5. 5. Photocell Temp. vs. I_0 , Productivity vs. I_0 .

Temperature at a photo cell panel is cooled with increase of flow. Then, electric output may increased but productivity of fresh water is decreased. The figure indicates a qualitative tendency of these relationship.

Water to power ratio for such a hybrid system may be a key factor to determine the optimum condition under the relationship. Water to power ratio has become a current topic in desalination and the trials are aimed to increase water production. Saudi Arabia having the biggest desalination facilities recently reported that the total capacity of desalination plants will be 565 MGD ($86,200 \text{ m}^3/\text{hr}$) with total 4,079 MW power plants in 1989. The average water to power ratio is estimated to be about $0.02 \text{ m}^3/\text{kW} \cdot \text{h}$. Let see again Fig. 5. 5, then the water to power ratio can read to be order of $0.6 \times 10^{-3} \text{ m}^3/\text{kW} \cdot \text{h}$ under an assumption that a practical conversion efficiency of photocell is of 10 %. This value is 30 % that of Saudi Arabian facilities. If the solar still is designed to be two effects or photo cell efficiency is improved to 20 %, the value will become 60 %. Many systems will be conceivable from the result. Now it becomes obvious that the hybrid system of the proposed solar still connected with photoelectric cell is quite promising to overcome both water and energy problems.

5. 5. Conclusion

The idea to improve the feeding system of a roof type solar still was proved to be feasible by using the laboratory test apparatus of two effects made from polyethylene film heated by infrared lamp.

The materials for constructing solar stills were discussed and a concept to substitute a panel of photoelectric cell for the heat receiving plate of a solar still. The hybrid system of the roof type solar still combined with the water to power ratio is a order of $0.6 \times 10^{-3} \text{ m}^3/\text{kW} \cdot \text{h}$ which is 30 % that of conventional dual purpose systems.

It can be concluded that the tested roof type solar still and the proposed hybrid system is quite promising and worthy to urgently develop.

6. Multieffect Solar Still for Agricultural Purposes in Hot Climate

6. 1. Introduction

A series of studies^{10,16,17,18,19)} has been conducted by the authors to develop a roof-type multieffect solar still. Experimentation and simulation created extensive knowledge of the heat and mass transfer in such type of solar stills and provided useful information about the design improvement and optimum operating conditions.

Several investigators^{20,21,22)} studied the feasibility of using basin-type stills to irrigate the inside of greenhouses, while this section deals with the possibility of using the roof-style multistage solar still for agricultural purposes in a hot climate on the basis of these performances.

6. 2. Design Concepts

Energy and mass flows in the multieffect solar still are shown in Fig. 6. 1. The specific point is that solar radiation is used to provide the heat of evaporation in the first effect. Then, the heat of condensation from the first effect is used to provide the heat of evaporation in the second effect, and so on. The condenser of the last effect is cooled naturally by ambient air. This type produces an amount of distillate approximately equal to the number of effects times the amount of distillate produced by an effect of the same area.

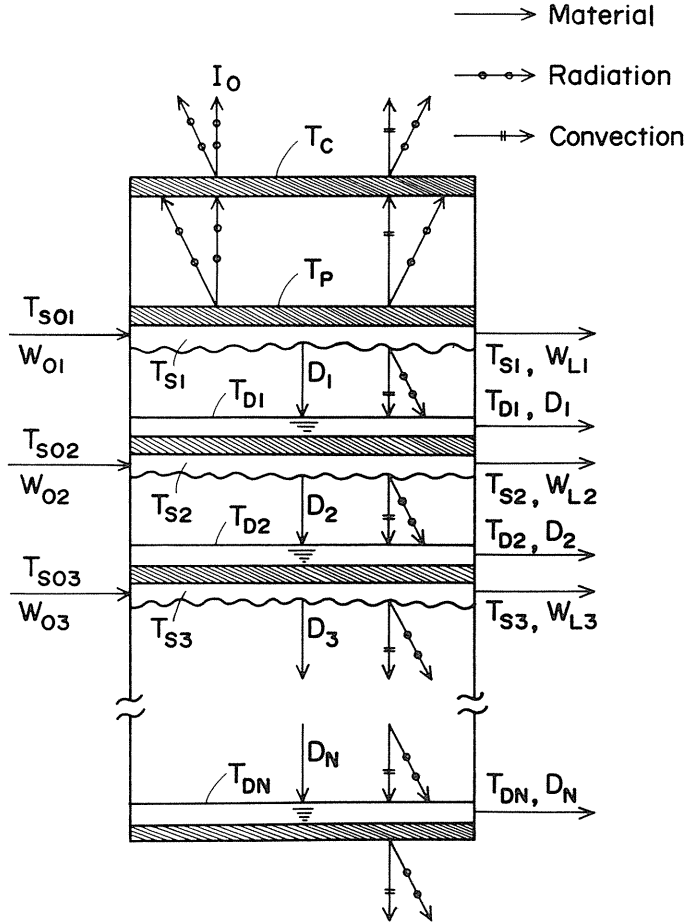


Fig. 6. 1. Heat and mass flows of the multi-effect solar stills.

The use of such a solar still for agricultural purposes in hot arid zones is effective because the construction cost is low and the operation requires no particularly technical skill. All Middle East countries have a great amount of solar radiation, which causes major problems for agriculture due to overheating of plants. Generally the major problem in arid regions is the shortage of water accompanied with excessive heat. Moreover, the radiation to the clear sky at night reduces the plant temperature to 10°C below the ambient temperature, which causes a shock in most plants. In many parts of arid zones, plants are protected against the night radiation by simple shelters made from palm leaves as shown in Fig. 6. 2.

To avoid overheating of plants, only the necessary amount of sunlight should be permitted to reach the plant. This amount can be expressed as²³⁾

$$\frac{\text{Required daylight}}{\text{Total daylight}} = \frac{(\text{Latitude in degrees})^{0.5}}{100}$$



Fig. 6. 2. Shelters made from palm leaves.

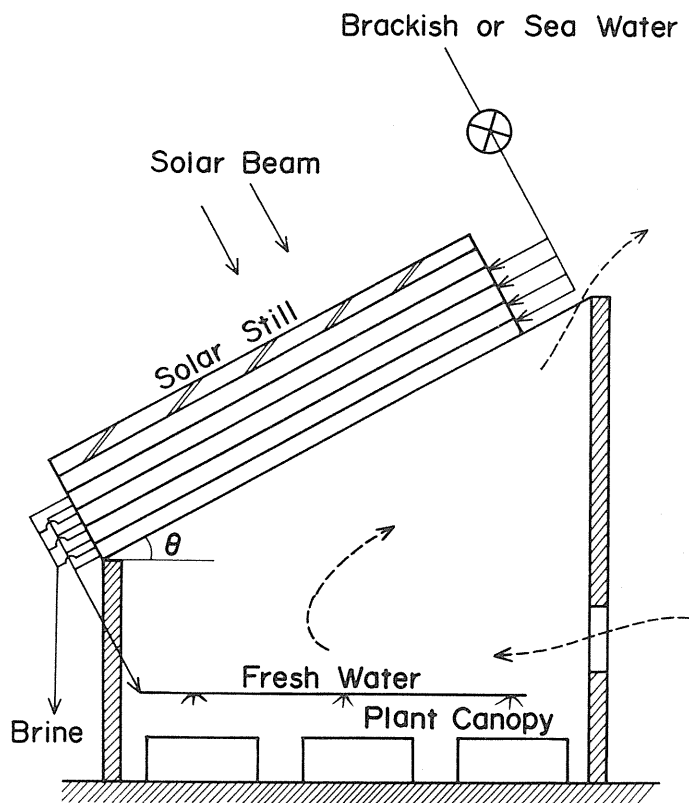


Fig. 6. 3. A greenhouse with a roof-type solar still.

For example, Riyadh (Saudi Arabia) is at latitude 25°N . Therefore the daylight required for plant growth in that area is 5 % of the total daylight. The roof-type solar still studied by the authors shelters the plants and dissipates sunlight. Design examples are shown in Fig. 6. 3. In this case, most of solar energy striking the roof of the greenhouse will be dissipated in the

processes of evaporation and condensation inside the stills, which ensures sufficient cooling inside the greenhouse.

Building walls made of limestone are less expensive and suitable for construction in the hot deserts of the Middle East area. Thus the southern and northern walls are made of limestone, since the maximum heat gain always comes from the south, and since the minimum gains come from the east and west, eastern and western walls are transparent in order to permit the required daylight for plant growth (after sunrise from the eastern wall and before sunset from the western wall). Vents are installed at suitable places to allow air circulation with a minimum heat gain from outside and suitable humidity inside the greenhouse. The water fed to the plants is enriched by a fertilizer and distributed by drip irrigation or perforated rubber tubes placed on the surface of the soil.

6. 3. Water Production Rate

6. 3. 1. Using a solar still as a simple shelter

The crop water requirement must be less than the total still production in order to irrigate without additional supply. The water consumption can be predicted if the reference crop evapotranspiration, ET_r , which is the sum of the rate of evaporation from the surface of the soil and the rate of transpiration from plants, is known. It is measured by using lysimeters or calculated empirically.²⁰⁾

Crop water requirements are obtained by multiplying ET_r by the crop coefficient K_C . The crop coefficient depends on the type of crop and the stage of growth. Typical values of K_C are shown in Table 6. 1.^{24,25)}

A certain arid place at the location of 34°39'N latitude and 46°39'E longitude in Saudi Arabia was taken as a case study. The weather conditions at this location, which are shown in Table 6. 2, were taken as input data to a dynamic simulation program of the multistage solar still.¹⁶⁾ Minimum feed rates required to safely operate the 5 stage solar still were estimated and are shown in Table 6. 3. The calculated distillate productivities of the still are shown in Fig. 6. 4 together with reference crop evapotranspirations at the same location²⁶⁾ and the crop

Table 6. 1. Crop coefficients for each stage of crop growing.

Crop development stage	Crop coefficient, K_C
Initial	0.3 – 0.4
Development	0.7
Midseason	1.1
Late season	0.9
Harvest	0.6 – 0.9

Table 6. 2. Ambient temperature (T_{amb}) and maximum solar radiation (I_{max}) in an arid area in Saudi Arabia.

	Jan.	Feb.	Mar.	Apl.	May	June	July	Aug.	Sep.	Oct.	Nov.	Dec.
I_{max} , W/m ²	590	644	741	796	810	807	805	797	795	686	606	568
T_{amb} , °C	28	28.5	30	31	33.5	35	33.5	31.5	30	28.5	27	25

Table 6. 3. Feed to the 5 stage solar still in an arid area in Saudi Arabia.

	Jan.	Feb.	Mar.	Apl.	May	June	July	Aug.	Spt.	Oct.	Nov.	Dec.
Feed, kg/h · m	3.75	4	5	5.5	6	6.25	6	5.75	5.25	4.75	4	35

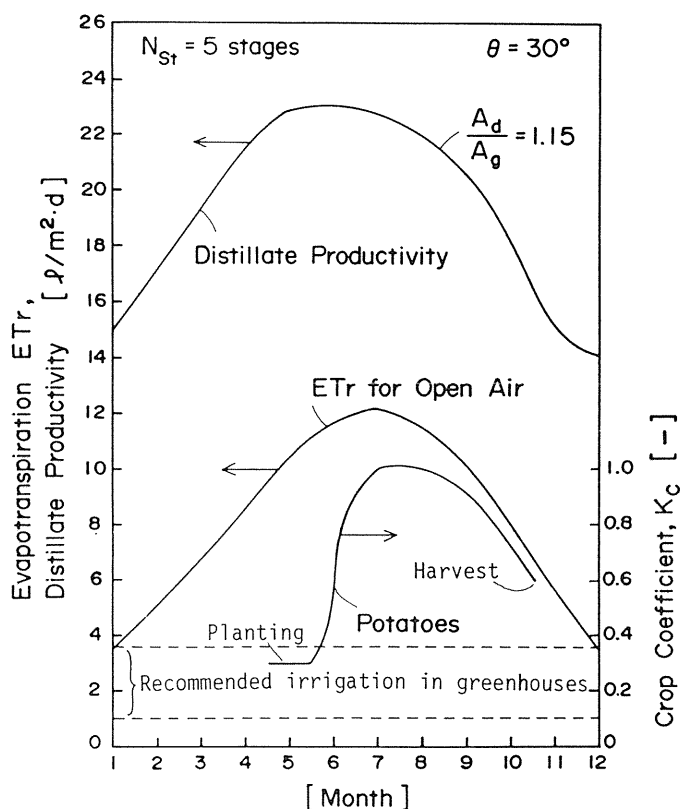


Fig. 6. 4. The calculated distillate productivity of a solar still, the evapotranspiration, and the crop coefficients for potatoes.

coefficient for potatoes. It can be seen from the figure that distillate productivities of the 5 stage still are 8 fold the crop consumption at initial crop stages, 2 fold at midseason, and 3.8 fold at harvest.

It should be noted that the still shelters the soil and plants sufficiently from the strong solar beam as shown in Fig. 6. 2, even if the given irrigation requirements would be lower than the values indicated in Fig. 6. 4. Moreover, the water production rate can be further increased by blending brackish water to the specified salinity level (500 ppm.) This increase will depend on salinity of the water source.

6. 3. 2. Using a solar still as roof for a greenhouse

Governing equations for heat and mass balances can be formulated by combining the solar still with a greenhouse. However, when the number of stages increases, the amount of heat rejection from the bottom stage to the greenhouse becomes negligible. Thus, the distillate productivities were calculated by using the simulator of a multistage solar still.^{10,16)} The water requirements for greenhouses were quoted from the data reported by other investigators, namely, the data for ET_r inside the greenhouse in Ankara, Turkey,²⁰⁾ was used in this study. The weather conditions there were also used for the simulation model. The calculated values of distillate productivity and their comparison with the values of daily ET_r inside the greenhouse²⁰⁾ are shown in Table 6. 4. It can be seen that the distillate productivity is ca. 13.5 ~ 17.5 fold the evapotranspiration inside the greenhouse.

Table 6. 4. Calculated values of daily ET_r in Ankara, Turkey, and their comparison with measured productivities of the solar still.

Run no.	Date	Method	Etr, mm/d ($1/m^2 \cdot d$)		Solar still production ($1/m^2 \cdot d$)	5 stage still ($1/m^2 \cdot d$)	Feed mm ($kg/h \cdot m$)
			Greenhouse	Outside			
2	21/8/71	Penman	0.61	0.95	3.8	—	—
		Rahrer	0.69	1.04			
3	24/8/71	Penman	0.69	1.65	4.3	13.04	3.5
		Rahrer	0.79	1.92			
4	11/9/71	Penman	0.85	1.05	3.3	12.3	3.25
		Rahrer	0.97	1.20			
6	16/9/71	Penman	0.89	1.60	3.0	—	—
		Rahrer	1.02	1.82			
7	29/9/71	Penman	0.76	1.35	2.4	—	—
		Rahrer	0.87	1.54			
8	12/10/71	Penman	0.55	1.30	1.8	—	—
		Rahrer	0.62	1.47			
9	13/10/71	Penman	0.27	0.99	1.9	—	—
		Rahrer	0.31	1.12			
10	14/10/71	Penman	0.44	1.18	1.8	8.41	2.25
		Rahrer	0.53	1.33			

No complete information about the water requirements inside greenhouses in very arid areas was reported, but O. Al Kasabi Tarek et al.²¹⁾ reported that the water required for a greenhouse system without counting the area required for walkways was 12 ~ 35 $m^3/day/$ hectare. This range is shown by dashed lines in Fig. 6. 4, together with the distillate productivity of a 5 stage solar still. It can be seen that the maximum distillate productivity is 10 fold the average value of the recommended irrigation range inside the greenhouse.

6. 4. Conclusion

The feasibility of utilizing the roof-type multistage solar still for agricultural purposes in hot arid zones was discussed. Conceptual designs which allow simple construction and easy operation without any particular technical qualifications were also discussed. The results

showed that when using the 5 stage solar still as a simple shelter for plants in hot arid climates in the Middle East, it can give a distillate productivity 8 fold the crop consumption at initial crop stages, 2 fold at crop mid-season, and 3.8 fold before crop harvest. When using the solar still as a roof for a greenhouse, the distillate productivity reaches almost 17 fold evapotranspiration inside the greenhouse in Anakra, Turkey. Thus, the suggested system is a self-supply system which can produce fresh water for the use of growing crops without additional water supplies from brackish or seawater and need for abundant sunshine.

Acknowledgements

The authors acknowledge Oriental Metal Mfg. Co. for contribution of the laboratory test plant and Water Reuse Promotion Center for the field test data. Gratitude is for The Salt Science Research Foundation with the financial support of this study.

References

- 1) M.A.S. Malik and V.M. Puri: Solar Energy, **14**, 371 (1973).
- 2) M.A.S. Malik, G.N. Tiwari, A. Kumar and M.S. Sodha: 'Solar Distillation', *Pergamon Press*, Oxford (1982).
- 3) K. Tsumura, M. Yamashita, M. Nishimura and T. Mishijima: 'Study on a Newly Developed Solar Disalination System', *Kukichowa-Eiseikogaku Ronbunshu*, A-40 (1980).
- 4) S. Toyama, T. Aragaki, K. Murase and K. Tsumura: 'Simulation of a Multieffect Solar Distillator', *Desalination*, **45**, 101 (1983).
- 5) S. Toyama, T. Aragaki, K. Murase, H.M. Salah and M. Sando: 'Simulation of Multistage Solar Distillator', *Proc. Annual Meeting of SCEJ*, Yokohama, p.336 (1985).
- 6) G.O.G. Lof, J.A. Eibling and J.W. Blowmer: 'Energy Balances in Solar Distillers', *AIChE J.*, **7** (4), 641 (1961).
- 7) S. Toyama: 'Multistage Flash Distillation', 'Kagaku Kikai Gijutsu, Vol.24', p.159, *Maruzen*, Tokyo (1972).
- 8) T. Hakuta, T. Goto and S. Ishizaka: 'Boiling Point Elevation of Sea Water', *Bull. Soc. Sea Water Sci.*, Japan, **28** (3), 156 (1974).
- 9) SCEJ (ed.): 'Kagaku Kogaku Binran', *Maruzen*, Tokyo (1978).
- 10) S. Toyama, T. Aragaki, H.M. Salah, K. Murase and A. Sando: 'Simulation of a Multieffect Solar Still and the Static Characteristics', *J. of Chem. Eng.*, Japan, **20** (5), 473 (1987).
- 11) S. Toyama, T. Aragaki, H.M. Salah and K. Murase: 'Heat and Mass Transfer during Evaporation from Free Surface of Water Flowing through Fibrous Sheet', *Proc. the 3rd World Congress of Chem. Eng.*, Tokyo, Vol.2, 522 (1986).
- 12) Japanese Patent Application, No. S.61-190212.
- 13) Catton: Adv. Heat Transfer Conference, Toronto, 1978, Vol.6, 13 (1979).
- 14) E.M. Sparrow and C. Prakash: 'Interaction between Internal Natural Convection in an Enclosure and an External Natural Convection JBoundary-Rayle Flow', *Int. J. Heat Mass Trans.*, **24** (5), 895 (1981).
- 15) S. Yoshida: 'Solar Energy Utilization Handbook', p.34, *Japan Solar Energy Soc.* (1985).
- 16) S. Toyama, T. Aragaki H.M. Salah and K. Murase: 'Dynamic Characteristics of a Multistage Thermal Diffusion Type Solar Distillator', *Desalination*, **67**, 21 (1987).
- 17) S. Toyama, T. Aragaki, H.M. Salah and K. Murase: 'Heat and Mass Transfer during Evaporation from a Free Surface of Water Flowing through Fibrous Sheet in an Inclined Enclosure', *J. of Chem. Eng.*, Japan, **20** (6), 579 (1987).

- 18) S. Toyama, M. Nakamura, H.M. Salah, S. Futamura and K. Murase: 'Laboratory JTest of Solar Distillator with a Heat Penetrating Plate Having a Bend', *Desalination*, **67**, 67 (1987).
- 19) M.S. Hassan: 'Studies on Multieffect Solar Still', *Ph.D. Thesis, Nagoya Univ.*, Nagoya, 1988.
- 20) M.K. Selcuk and V.V. Tran: *Sol. Energy*, **17**, 103 (1975).
- 21) T.O. Al Kasbi, S.I. Abdel-Khalik, T.E. Dix, R. Hagenson, A.A. Husseiny and G.P. McLagan: 'Design of a Commercial Solar-Powered Greenhouse', *Desalination*, **39**, 53 (1981).
- 22) C.N. Tiwari, N.K. Dhiman: *Energy Convers. Manag.*, **25** (2), 217 (1985).
- 23) A.E. Dixon and J.D. Leslie, 'Solar Energy Conversion', p.1145, *Pergamon Press* (1979).
- 24) J. Doorenbos and Pruitt: *Irrigation and Drainage Paper 24*, p.156, *FAO*, Rome (1977).
- 25) J. Doorenbos and A.H. Kassan: *Irrigation and Drainage Paper 24*, p.156, *FAO*, Rome (1977).
- 26) M.A. Salih Abdin and M. Uyger Sendil: *Irrig. Drain.*, **110** (3), (1984).